M.B. Khanvilkar[1,2], A.K. Nikumbh[2], S.M. Patange[3], R.A. Pawar[2], N.J. Karale[2],
D.V. Nighot[2], P.A. Nagwade[2], M.D. Sangale[2], G.S. Gugale[2]

Structural, Electrical and Magnetic Properties of Substituted Pyrochlore Oxide Nanoparticles Synthesized by the Co-Precipitation Method

[1]*K.M.C. College, Khopoli, Tal-Khalapur, Dist. Raigad, India, mb.khanvilkar@gmail.com*
[2]*Savitribai Phule Pune University (Formerly University of Pune), Ganeshkhind, Pune, India, aknik1952@gmail.com*
[3]*Shrikrishna Mahavidyalaya, Gunjoti, Tal- Omerga, Dist. Osmanabad, India, smpatange@rediffmail.com*

Five substituted pyrochlore nanooxides such as $Nd_{1.9}Ho_{0.1}Zr_{1.8}Ce_{0.2}O_7$, $La_{1.95}Ce_{0.05}Zr_{0.29}Ce_{1.71}O_7$, $Y_{1.79}Pr_{0.21}Ru_{1.99}Pr_{0.01}O_7$, $Dy_{1.9}Yb_{0.1}Mn_{1.93}Cu_{0.07}O_7$ and $Dy_{1.99}Sr_{0.01}Sn_2O_7$ were synthesized by coprecipitation method. These precursors were monitored by thermal studies (TGA-DTA). The prepared nanosized substituted pyrochlore oxides were characterized by EDS, XRD, SEM, TEM, d. c. electrical conductivity, Thermoelectric power, Hall effect measurement, dielectric properties and magnetization measurements. XRD confirmed the formation of a single phase crystalline substituted pyrochlores with a cubic nature of nanoparticles. All substituted compounds were adopted a stable pyrochlore structure with r_A^{3+}/r_B^{4+} = 1.395 except $La_{1.95}Ce_{0.05}Zr_{0.29}Ce_{1.71}O_7$ compound, which has r_A^{3+}/r_B^{4+} = 1.175 indicate disorder pyrochlore structure (i.e. fluorite structure). The temperature dependence of d. c. electrical conductivity for all substituted pyrochlores exhibits two distinct slopes with a break. This discontinuity can be attributed to extrinsic to intrinsic semiconducting properties. The thermoelectric power and Hall effect measurements for all compounds were confirmed the p-type semiconductivity except $Y_{1.79}Pr_{0.21}Ru_{1.99}Pr_{0.01}O_7$ compound and which showed n-type semiconductivity. The dielectric constant (ϵ') and dielectric loss (tan δ) i. e dissipation factor decreases with an increase in frequencies and reaching constant at particular frequencies. The applied field dependence of magnetization curve at room temperature (300 K) for $Nd_{1.9}Ho_{0.1}Zr_{1.8}Ce_{0.2}O_7$, $Y_{1.79}Pr_{0.21}Ru_{1.99}Pr_{0.01}O_7$ and $Dy_{1.9}Yb_{0.1}Mn_{1.93}Cu_{0.07}O_7$, showed hysteresis loop with a small kink around the origin and which can be attributed to small but definite ferromagnetic ordering along with significant paramagnetic and superparamagnetic components. The magnetization at 2K showed a clear hysteresis loop for $Dy_{1.9}Yb_{0.1}Mn_{1.93}Cu_{0.07}O_7$ and $Dy_{1.99}Sr_{0.01}Sn_2O_7$ pyrochlores are soft (weak) ferromagnets.

Keywords: substituted pyrochlore-type oxides, ferromagnetism, electrical conductivity, magnetization, exchange interaction, coprecipitation.

Received 17 March 2021; Accepted 7 June 2021.

Introduction

Recently, pyrochlore-type oxides ($A_2B_2O_7$) with the cubic structure are the most important among ceramic materials because they show a high geometric frustration on both A and B sublattices [1, 2]. In this structure, large cations such as lanthanides (Ln) typically occupy the A site, which is coordinated to eight oxygen ions, where the B site fits better with smaller transition elements of the first or second row and which are coordinated to six oxygen ions in an almost octahedral environment. When the Ln cation is paired with the diamagnetic B^{4+} cation, the most favorable condition occurs for studying lanthanide magnetism. In a pyrochlore formula of $A_2^{3+}B_2^{4+}O_7^{2-}$, the choice is then limited to Sn^{4+} and marginally to Zr^{4+} or Ce^{4+}, which form pyrochlore compounds with fewer $Ln_2Ti_2O_7$ lanthanides which have

been widely studied [2].

The pyrochlore-type oxide formula is $A_2B_2O_7$ or $A_2B_2O_6O'$. These oxides with the Fd3m space group crystallize in cubic lattices. Trivalent lanthanide, divalent alkaline earth, or monovalent alkali ions may occupy A site with 8 coordinates. Site B can be filled for charge neutrality by six-coordinate tetravalent (Ti^{4+}, Zr^{4+}, Ru^{4+}, Sn^{4+}) etc or pentavalent (Nb^{5+}, Ta^{5+}) ions. The structure of the $A_2B_2O_6O'$ has distorted BO_6 octahedra that share corners to form a tetrahedral B_2O_6 formula lattice [1]. At the center of the hexagonal oxygen rings (formed from six BO_6 octahedra), the A cations are present with two more oxygen (O') located above and below the rings and are thus eight-coordinated. Each O' atom is tetrahedrally coordinated with A cations, and the A and O atoms form a tetrahedral lattice formula A_2O'. B_2O_6 and A_2O' lattices interpenetrate and via B-O-A relations, the B and A cations interact. Each O is surrounded by two B and two A cations in a distorted tetrahedron. The $A_2B_2O_6O'$ pyrochlore tolerates a high degree of vacancy at the sites of the O' anion, so its composition is $A_2B_2O_6(O')_{1-y}$ i.e. $A_2B_2O_{7-y}$ if the distinction between O and O' is not rendered [1].

With 3m symmetry, the A and B cations occupy 16d and 16c positions respectively. With 2mm symmetry, the oxygen ions occupy 48f (x, 1/8, 1/8) while O' occupies 8b site with 43m symmetry. Site 8a will be symmetrically empty. A superstructure of defect fluorite (Fm 3m space group) with twice the lattice constant is the ordered pyrochlore structure [1, 2]. Due to the presence of anion vacancies and the short ordering of A and B cations, the ideal defect fluorite structure is rarely obtained. The oxygen position of 48F is displaced and its magnitude is given by positional parameter x, which for the pyrochlore structure is in the range 0.3125 - 0.3750. The formation of defects in complex oxides is very important for advanced materials to be rationally produced. The structure of the oxides of $A_2B_2O_7$ strongly depends on the cation radius ratio of r_A^{3+} / r_B^{4+} [3-4]. The defect formation energies of a large number of pyrochlore compositions have been determined by several experimental observations of the pyrochlore system [5-6], which indicate that the ionic size variation at B-site has a comparatively greater effect on the ionic size variation at A-site in deciding the defect formation energies. The difference in the ionic size of the A-site ion also has enough importance for pyrochlore stability [7, 8].

In catalysis [9, 10], electrode materials in solid oxide fuel cells [11, 12] and nuclear waste [13], lithium ion batteries [14], phosphors [15], and thermal barrier coatings [16], pyrochlore oxides have been commonly used. The essential applications are related to the migration of oxygen between specific sites of oxygen [5, 17]. The semiconducting properties of Pr, Gd and Bi pyrochlore oxides at the A-site and Zr, Ce, Sn, In, Mo, Ti at the B-site were found to have a high intrinsic semiconductor level due to anion disorder, which was consistent in compounds with the cation radius ratio r_A /r_B [18-21]. Due to their fascinating electrical insulator properties, rare earth ruthenate compounds have been studied in the past decade [22]. Other ruthenate pyrochlores, such as $Bi_2Ru_2O_7$ and $Pb_2Ru_2O_7$, are

metallic, while $Bi_{2-x}Ln_xRu_2O_7$ and $Pb_{2-x}Ln_xRu_2O_7$ (Ln = y, La, Nd) are semiconductors [23, 24]. The magnetic properties of $Ln_2Ru_2O_7$ (Ln = Pr, Sm, Gd, Tb, Dy, Ho, Er, Tm and Yb) heavy rare earth ruthenate pyrochlore showed antiferromagnetic to paramagnetic transition temperature to around 60 - 120 K. Although $Gd_{2-x}M_xRu_2O_7$ and $Y_{2-x}M_xRu_2O_7$ (M=Co, Ho, Y, Pr) pyrochlore magnetic properties of substituted ruthenate showed antiferromagnetic to ferromagnetic properties [25-27]. Likewise its magnetic phase transition, $Ln_2Mn_2O_7$ rare earth manganese pyrochlores differ as compared to other pyrochlore oxide systems such as $Ln_2Mo_2O_7$ and $Lu_2Ru_2O_7$, which display ferromagnetic semiconductors [28-32]. The effects of magnetic dilution in the ferromagnetic manganese pyrochlore system $(Dy_{1-x}Ln_x)_2Mn_2O_7$ and $(Y_{1-x}Ln_x)_2Mn_2O_7$ (Where Ln^{3+} = Lu^{3+}, Yb^{3+}) were also studied to investigate the role of Ln^{3+} ionic size versus 4f moment on the magnetic properties of Mn^{4+} sublattices [31, 33, 34]. Furthermore, the low temperature magnetic properties of rare earth stannates ($Ln_2Sn_2O_7$) in which the Sn (IV) ion is non-magnetic and the magnetic interaction change is caused by a lattice parameter difference in the same rare earth elements [35-37]. As a function of temperature and oxygen partial pressure, the semiconductive activity of $Sr_{2x}Ce_{2-2x}Sn_2O_7$ and $Ln_2Sn_{2-x}B_xO_7$ (B= Fe, Co, Ni) with a cubic pyrochlore structure was calculated [36-38]. Many studies have recently been published on iridium-based pyrochlore oxides such as $A_2Ir_2O_7$, where, due to its new topological process, A is a trivalent rare earth element or bismuth that has attracted considerable interest [39-42].

For the synthesis of pyrochlore oxides, numerous types of methods have been identified, such as solid-state reactions [43], coprecipitation [44], sol-gel [45], hydrothermal [46] and hydrazine [47]. The solid-state method involves a very high temperature for a long time and a small yet measurable amount of impurity has been obtained. On the other hand, the process of co-precipitation is more eco-friendly than other approaches. Hence it is available at significantly lower temperatures to produce a pure crystalline phase with high chemical homogeneity and stoichiometric nano-sized pyrochlore oxides.

Inspired by above mentioned investigation, as different transition and or rare earth elements dopants, in general, are different in sizes, in pyrochlore oxides inevitably involves some local structural changes and magnetic properties may affect the nature of the superexchange interactions. In the present paper, we report the substituted pyrochlore type nano oxides were synthesized by a simple tartrate or hydroxide coprecipitation method. In addition, we attempted to determine the effect of substituent's on structural, electrical and magnetic properties of some pyrochlore oxides, $A_{2-x}M_xB_{2-y}M'_yO_7$ (where M, M' = transition or rare earth elements). The character of the as-synthesized substituted pyrochlore material was characterized by X-ray diffraction (XRD), Transmission electron micrographs (TEM), semiconducting, and dielectric and magnetization measurements.

I. Experimental

1.1. Synthesis of precursors

All chemicals were of the highest purity available and the amounts of metal salts were determined based on stoichiometry in the final product as obtained with further purification. As a solvent, double distilled water was used. In all the experiments, clean glassware was used.

1.1.1. Holmium-neodymium-zirconium-cerium tartrate eight hydrates, $(Nd_{1.9}Ho_{0.1}Zr_{1.8}Ce_{0.2})O_2 (C_4H_4O_6)_5.8H_2O$

The mixing of $HoCl_3$ (0.1788 g), $NdCl_3$ (1.4868 g), $ZrOCl_2.8H_2O$ (1.7000 g) and $Ce (NO_3)_3.6H_2O$ (0.5965 g) in double distilled water formed a homogeneous solution. The solution's pH was changed to a sufficiently low value (pH < 5). Ammonium tartrate (3.9446 g dissolved in 25 mL distilled water) was progressively applied to this homogeneous solution by stirring until a permanent precipitate at 70 °C occurred. In similar quantities, acetone was added to the above solution to produce a more homogeneous, stoichiometric, fine grained powder.

The resulting precipitate was painted white. The solution was filtered for 30 minutes after it had been stirred. To accelerate the drying, the precipitate was washed with cold distilled water and then with acetone. At ambient temperature, it was air-dried. The flow sheet diagram for the precursor and subsequent conversion into nanooxides of the substituted pyrochlore form is shown in Fig.1.

For the synthesis of other precursors, a similar method was used by taking stoichiometric quantities of the respective salts. The additional information is given below.

1.1.2. Lanthanum-zirconium-cerium tartrate eight hydrates, $La_{1.95}Ce_{0.05}Zr_{0.29}Ce_{1.71}O_{0.5} (C_4H_4O_6)_6 .8H_2O$

In double distilled water, $La (NO_3)_3.3H_2O$ (2.3781 g), $ZrOCl_2.8H_2O$ (0.5284 g) and $Ce (NO_3)_3.6H_2O$ (2.2252 g) were dissolved. Then, drop by drop, with stirring, ammonium tartrate solution (4.1030 g dissolved in 50 mL distilled water) was introduced until a white precipitate was produced. For five minutes, the precipitate was digested, accompanied by filtration and washed with distilled water and acetone. It was air-dried at room temperature.
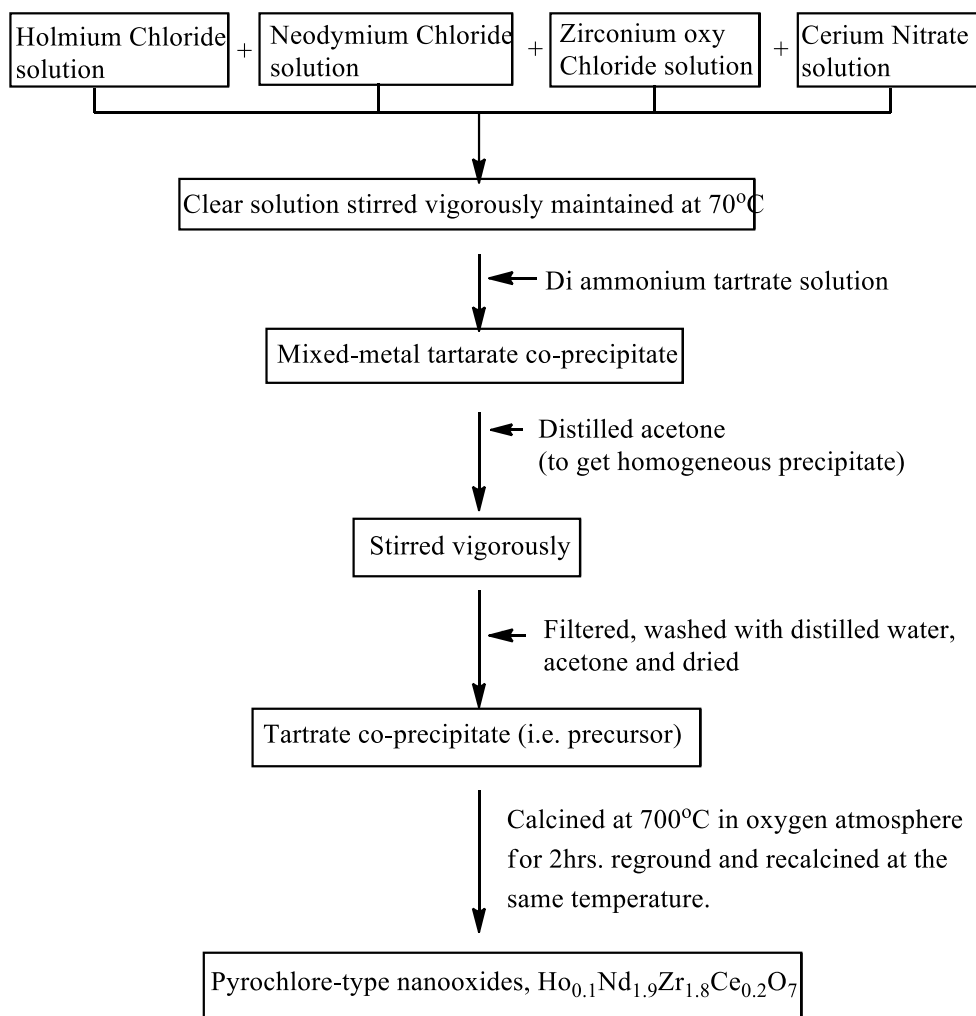
Fig. 1. Flow chart for synthesis of Holmium-Neodymium-Zirconium-Cerium pyrochlore, $(Nd_{1.9}Ho_{0.1}Zr_{1.8}Ce_{0.2})O_2(C_4H_4O_6)_5.8H_2O$.

1.1.3. Yttrium-praseodymium-ruthenium tartrate seven and a half hydrate, $Y_{1.79}Pr_{0.21}Ru_{1.99}Pr_{0.01}$ $(C_4H_4O_6)_6$ .7.5H_2O

Similarly, Y $(NO_3)_3$.5H_2O (2.4451 g), Pr $(NO_3)_3$.6H_2O (0.5143 g) and $RuCl_3$ (1.6348 g) were administered in double distilled water following the above method. Stir and then slowly apply the ammonium tartrate solution (5.4401 g dissolved in 50 mL distilled water) unless there is a permanent gray precipitate. The precipitate was filtered and washed at room temperature with distilled water and acetone, and air dried.

1.1.4 Dysprosium - Ytterbium - manganese - copper tartrate tetra hydrate, $Dy_{1.9}Yb_{0.1}Mn_{1.93}Cu_{0.07}$ $(C_4H_4O_6)_5$ .4 H_2O

In double distilled water, a mixture of Dy $(NO_3)_3$.6H_2O (2.697 g), Yb $(NO_3)_3$.6H_2O (0.6898 g), $MnCl_2$.4H_2O (1.9236 g) and $CuCl_2$.2H_2O (0.1562 g) was dissolved. The pH of the medium was modified to a low enough value (pH < 6) to avoid the formation of hydroxide precipitates. It was slowly applied with ammonium tartrate solution (4.0161g dissolved in 25 mL distilled water) with regular stirring until a slight green precipitate was produced. Then with cold distilled water and acetone, it was filtered and washed. The precursor was dried at ambient temperature.

1.1.5. Dysprosium-Strontium-tin hydroxide, $Dy_{1.99}Sr_{0.01}Sn_2$ $(OH)_{14}$

0.6721 g $SnCl_2$.2H_2O was dissolved in 5mL of concentrated hydrochloric acid (HCl) and boiled to form a solution of $SnCl_4$ and purified water dilute the above solution to 25 mL. An aqueous solution of $(NH_4)_2Sn$ $(OH)_6$ complex was prepared by the gradual addition of NH_4OH (1mol/L) to above $SnCl_4$ aqueous solution, till the precipitation of Sn $(OH)_4$. To get a simple solution of $(NH_4)_2$ Sn $(OH)_6$, add excess NH_4OH.

A mixture of Dy $(NO_3)_3$.6H_2O (1.3329 g) and $SrCl_2$.6H_2O (0.0159 g) was dissolved into 50 mL of distilled water in another vessel. In order to get a permanent coprecipitates, $(NH_4)_2$ Sn $(OH)_6$ solution was slowly added with stirring to the above mixture. Here the pH of the medium was changed to a sufficiently high value (pH: 11) to complete the precipitation of hydroxide. After digesting it at 70 °C for one hour, the white precipitate was filtered. The precipitate was washed several times, until neutral to pH paper, with cold distilled water. It was air-dried at room temperature.

1.2. Synthesis of substituted pyrochlore - type nanooxides

The above tartrate and hydroxide precursors were decomposed and slowly calcinated under a oxygen air atmosphere at 700 °C for two hours in a platinum crucible and then slowly cooled down to room temperature (3°C/min). This heat treatment was sufficient to achieve the total decomposition of tartrate/ hydroxides. The obtained powder was re-ground and re-calcined for another two hours at the same temperature. The furnace was turned off and at room temperature, the sample was removed. The substituted pyrochlore oxides obtainable were restored in a desiccator, such as $Nd_{1.9}Ho_{0.1}Zr_{1.8}Ce_{0.2}O_7$, $La_{1.95}Ce_{0.05}Zr_{0.29}Ce_{1.71}O_7$, $Y_{1.79}Pr_{0.21}Ru_{1.99}Pr_{0.01}O_7$, $Dy_{1.9}Yb_{0.1}Mn_{1.93}Cu_{0.07}O_7$ and $Dy_{1.99}$ $Sr_{0.01}Sn_2$ O_7.

1.3. Characterization technique

The content of carbon and hydrogen was measured using a microanalytical technique. Inductively coupled plasma spectrometer (ICP-AES instrument ARCOS from M/S. spectro Germany) and Energy dispersive X-ray analysis (EDS) on SEM PHILIPS XL 30 CP instruments were used for determining the chemical composition of the substituted sample. The IR (4000 - 450 cm^{-1}) spectra of the compounds were reported using the KBr disk technique using the PerkinElmer IR 1600 spectrophotometer. With a Mettler Toledo 850 thermal analyzer, TGA and DTA were performed at 10 °C min^{-1} in static air.

By powder X-ray diffraction (XRD), the phase identification of synthesized substituted pyrochlores can be achieved. On the Siemens D500, this XRD pattern was detected. The morphology analysis of substituted pyrochlores can be performed on a JEOL-2010 transmission electron microscope, working at an accelerating voltage of 208 kV, using transmission electron microscopy (TEM) and the corresponding selected area electron diffraction (SAED) pattern. The semiconducting properties of all samples were determined by d. c. electrical conductivity, thermoelectric power and Hall effect measurements on the ECOPIA (HMS3000) instrument with a constant magnetic field of 5 Tesla (τ). The dielectric properties of substituted pyrochlores were tested using a HIOKI model 3532-50 LCR Hi Tester at room temperature (frequency range from 100 Hz to 5 MHz). Elsewhere in the literature, the technique used for these measurements was defined [48].

Using a SQUID magnetometer, the magnetic nature of substituted pyrochlores was reported (Quantum Design MPMS-55). In the temperature range 5 to 325 K and in the constant field 100 Oe, sample magnetization was carried out in the field cooling i.e. FC (in the estimation field) and zero fields cooling i.e. ZFC (in absence of a field). The magnetization was also measured using a PAREG and G model No.4508 vibrating sample magnetometer with an applied field of up to 20 k Oe as a function of the applied field at room temperature.

II. Results and discussion

2.1. Characterization of precursors

The metal and (C, H) content of tartrate and hydroxide precursors were made in wt % for $Nd_{1.9}Ho_{0.1}Zr_{1.8}Ce_{0.2}O_2$ $(C_4H_4O_6)_5$.8H_2O, (C,cal.17.14 and found 16.89; H cal.2.57 and found 2.59 ;Nd, cal.19.57 and found 18.98; Ho, cal.1.18 and found 1.74; Zr, cal.11.73 and found 12.17; Ce, cal. 2.00 and found 1.84); $La_{1.95}Ce_{0.05}Zr_{0.29}Ce_{1.71}O_{0.5}(C_4H_4O_6)_6$. 8$H_2O$, (C,cal.18.84 and found 19.07; H, cal.2.53 and found 3.02; La, cal.16.34 and found 17.91; Ce, cal.14.88 and found 14.16; Zr, cal. 1.60 and found 1.57); $Y_{1.79}Pr_{0.21}Ru_{1.99}Pr_{0.01}(C_4H_4O_6)_6$ .7.5H_2O, (C,cal.20.39 and found 20.55; H cal.2.76 and found 2.34 ; Y, cal.11.26 and found 11.81; Pr, cal.2.19 and found 2.04; Ru, cal.
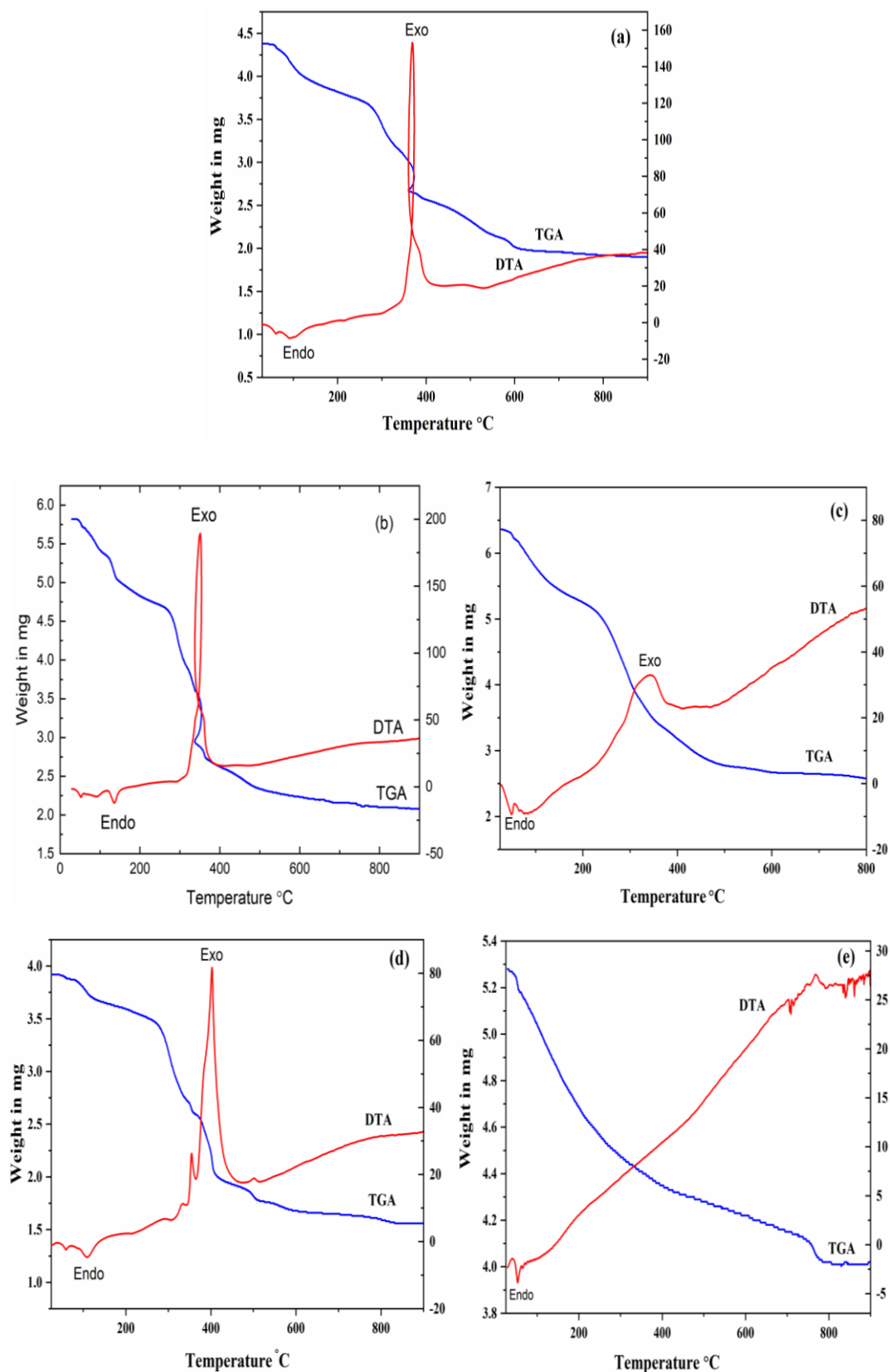
Fig. 2. TGA and DTA curves for tartrate / hydroxide precursors in normal air atmosphere.
(a) $(Nd_{1.9}Ho_{0.1}Zr_{1.8}Ce_{0.2})O_2(C_4H_4O_6)_5.8H_2O$; (b) $La_{1.95}Ce_{0.05}Zr_{0.29}Ce_{1.71}O_{0.5}(C_4H_4O_6)_6\ 8H_2O$;
(c) $Y_{1.79}Pr_{0.21}Ru_{1.99}Pr_{0.01}(C_4H_4O_6)_6\ .7.5H_2O$; (d) $Dy_{1.9}Yb_{0.1}Mn_{1.93}Cu_{0.07}(C_4H_4O_6)_5\ .4H_2O$,
(e) $Dy_{1.99}Sr_{0.01}Sn_2(OH)_{14}$

Table 1

TGA and DTA data of tartrate / hydroxide precursors under normal air atmosphere

Precursors	TGA			DTA peak temp. (°C)	Predicted intermediates and final products
	% mass loss		Temp. range (°C)		
	Observed	Calculated			
$Nd_{1.9}Ho_{0.1}Zr_{1.8}Ce_{0.2}O_2$ $(C_4H_4O_6)_5.8H_2O$	10.62	10.05	35-220	90	$Nd_{1.9}Ho_{0.1}Zr_{1.8}Ce_{0.2} O_2(C_4H_4O_6)_5$
	55.25	52.98	220-601	350	$Nd_{1.9}Ho_{0.1}Zr_{1.8}Ce_{0.2}O_7$
$La_{1.95}Ce_{0.05}Zr_{0.29}Ce_{1.71}O_{0.5}$ $(C_4H_4O_6)_6$ $8H_2O$	9.3	8.32	35-190	140	$La_{1.95}Ce_{0.05}Zr_{0.29}Ce_{1.71}O_{0.5} (C_4H_4O_6)_6$
	54.98	53.66	190-600	380	$La_{1.95}Ce_{0.05}Zr_{0.29}Ce_{1.71}O_7$
$Y_{1.79}Pr_{0.21}Ru_{1.99}Pr_{0.01}$ $(C_4H_4O_6)_6$ $.7.5H_2O$	59.12	64.23	40-180	95	$Y_{1.79}Pr_{0.21}Ru_{1.99}Pr_{0.01} (C_4H_4O_6)_6$
	37.13	36.53	180-345	300	$Y_{1.79}Pr_{0.21}Ru_{1.99}Pr_{0.01} (CO_3)_7$
	19.04	18.89	345-491	430	$Y_{1.79}Pr_{0.21}Ru_{1.99}Pr_{0.01}O_7$
$Dy_{1.9}Yb_{0.1}Mn_{1.93}Cu_{0.07}$ $(C_4H_4O_6)_5$ $.4H_2O$	6.12	5.75	25-180	110	$Dy_{1.9}Yb_{0.1}Mn_{1.93}Cu_{0.07} (C_4H_4O_6)_5$
	54.17	53.21	180-600	420	$Dy_{1.9}Yb_{0.1}Mn_{1.93}Cu_{0.07}O_7$
$Dy_{1.99}Sr_{0.01}Sn_2(OH)_{14}$	18.69	15.81	35-600	50	$Dy_{1.99}Sr_{0.01}Sn_2O_7$

Table 2

Observed ICPEs and EDS analysis of substituted pyrochlore-type nanooxides

Substituted pyrochlore oxides	Formula Wt. (g Mol⁻¹)	Elemental analysis in wt % (±0.5)							
		Req	Found	Req	Found	Req	Found	Req	Found
$Nd_{1.9}Ho_{0.1}Zr_{1.8}Ce_{0.2}O_7$	594.77	Ho		Nd		Zr		Ce	
		2.77	2.33 (2.66)	46.08	46.89 (45.96)	27.61	27.97 (28.28)	4.71	4.57 (5.18)
$La_{1.95}Ce_{0.05}Zr_{0.29}Ce_{1.71}O_7$	655.93	La		Zr		Ce		--	
		41.30	41.98 (42.01)	4.03	4.14 (4.41)	37.60	37.01 (36.60)	--	--
$Y_{1.79}Pr_{0.21}Ru_{1.99}Pr_{0.01}O_7$	503.34	Y		Pr		Ru			
		31.62	31.75 (32.60)	6.16	5.83 (5.16)	39.97	40.24 (39.75)	--	--
$Dy_{1.9}Yb_{0.1}Mn_{1.93}Cu_{0.07}O_7$	548.81	Dy		Yb		Mn		Cu	
		56.26	56.71 (56.63)	3.15	3.00 (3.24)	19.32	18.98 (19.10)	0.81	0.88 (0.46)
$Dy_{1.99}Sr_{0.01}Sn_2O_7$	673.63	Dy		Sr		Sn		--	
		48.01	47.78 (48.16)	0.13	0.15 (0.12)	35.24	35.39 (34.98)	--	--

The figures in parenthesis indicate metal analysis obtained from EDS method

14.23 and found 14.34); for $Dy_{1.9}Yb_{0.1}Mn_{1.93}Cu_{0.07}(C_4H_4O_6)_5$ $.4H_2O$ (C,cal.19.24 and found 18.98; H cal.2.24 and found 2.17 ; Dy, cal.24.72 and found 25.15; Yb, cal. 1.39 and found 1.02; Mn, cal. 8.49 and found 9.43;Cu, cal.0.36 and found 0.36); for $Dy_{1.99}Sr_{0.01}Sn_2 (OH)_{14}$ (H cal.1.76 and found 1.33 ; Dy, cal.40.43 and found 40.64; Sr, cal.0.11 and found 0.13; Sn, cal. 29.69 and found 29.25). The presence of water of crystallization for these precursors was confirmed based on thermogravimetric analysis (TGA) under normal air atmosphere.

The infrared spectrum showed frequency corresponding to the tartrate group, hydroxyl group, metal - oxygen bonds etc. The infrared spectrum of tartrate precursors showed a broad band at 3357 cm⁻¹ corresponding to the weakly bonded water of crystallization, and the intense band at 1592 cm⁻¹ due to $\nu_{asy.}$ (C = O) and band at 1399 cm⁻¹ and 1260 cm⁻¹ due to $\nu_{sy.}$ (C–O).The bidentate linkage of tartrate group with metal was confirmed based on the difference between ν_{asy} and ν_{sy} stretching frequencies. There was no bonding with secondary –OH group (of d-tartaric acid) to metal in solid state. These values indicate the presence of coordinated carboxylate group. Chain – like polymeric octahedral structures have been assigned to this precursor [49, 50]. The infrared spectrum of hydroxide precipitate such as $Dy_{1.99}Sr_{0.01}Sn_2 (OH)_{14}$ showed characteristics vibrations at around at 3367 cm⁻¹ and 843 cm⁻¹ respectively assigned to stretching (ν_{OH}⁻) and vibrational lattice mode, ν_{M-OH} (deformed). The thermal profiles (TGA and DTA) of tartrate and hydroxide precursors in static air atmosphere from 30 - 700°C are shown in Fig. 2.

The thermal curves reveal two decomposition steps. The first step corresponding to dehydration and the second step corresponding to oxidative decomposition to produce respective substituted pyrochlore oxides. The observed mass losses and corresponding temperature ranges for TGA and endothermic or exothermic peak for DTA are shown in Table 1.
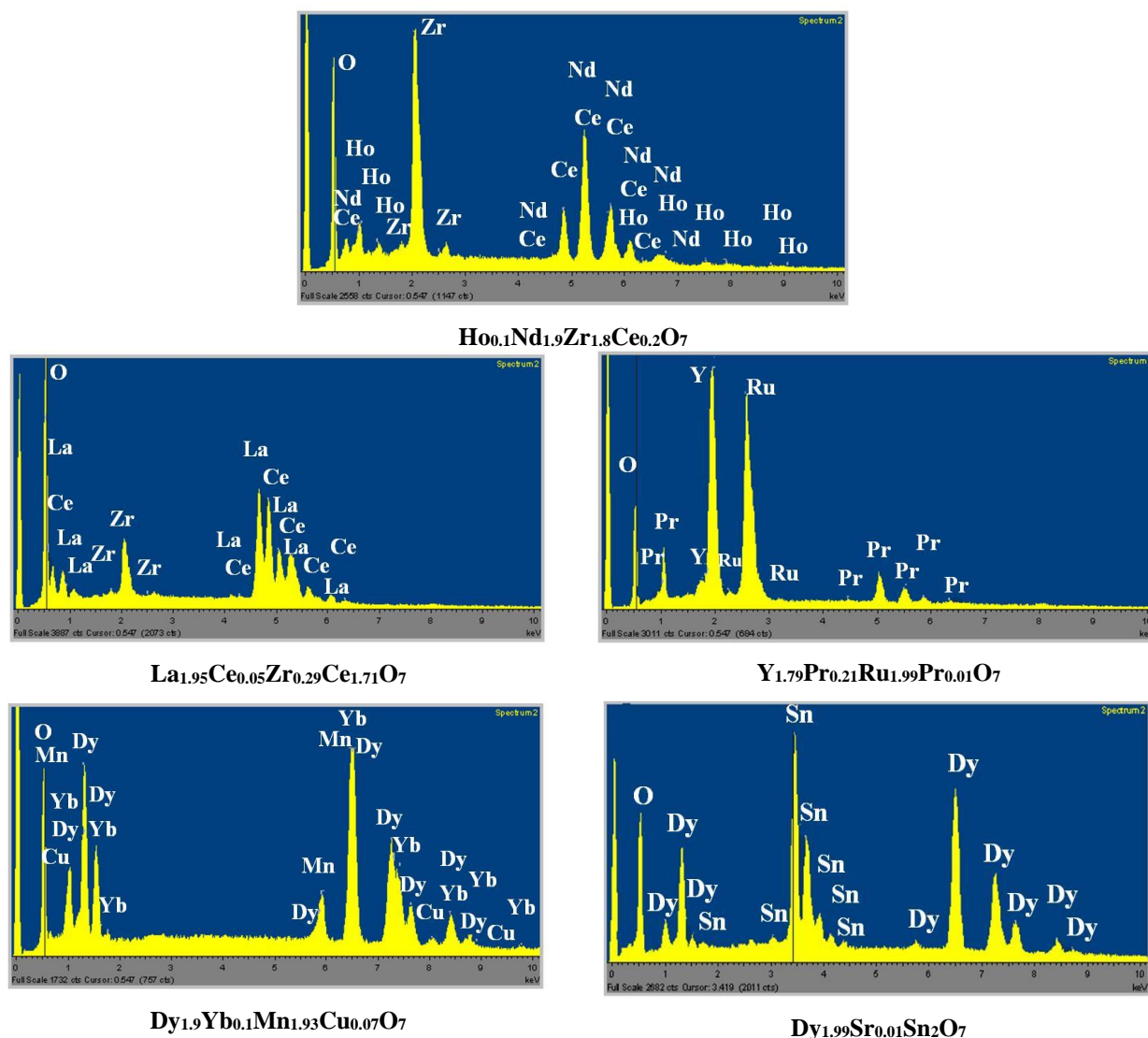
$Ho_{0.1}Nd_{1.9}Zr_{1.8}Ce_{0.2}O_7$

$La_{1.95}Ce_{0.05}Zr_{0.29}Ce_{1.71}O_7$

$Y_{1.79}Pr_{0.21}Ru_{1.99}Pr_{0.01}O_7$

$Dy_{1.9}Yb_{0.1}Mn_{1.93}Cu_{0.07}O_7$

$Dy_{1.99}Sr_{0.01}Sn_2O_7$

Fig. 3. Energy dispersive X-ray spectrum (EDS) of substituted pyrochlore-type nanooxides.

2.2. Characterization of substituted pyrochlore nanooxides.

2.2.1. Structural studies

As synthesized tartrate or hydroxide precursors were calcined in an oxygen atmosphere at 700 °C for two hours to produce respective substituted pyrochlore oxides. These oxides are then reground and recalcined at the same temperature for another two hours. The obtained samples such as $Nd_{1.9}Ho_{0.1}Zr_{1.8}Ce_{0.2}O_7$, $La_{1.95}Ce_{0.05}Zr_{0.29}Ce_{1.71}O_7$, $Y_{1.79}Pr_{0.21}Ru_{1.99}Pr_{0.01}O_7$, $Dy_{1.9}Yb_{0.1}Mn_{1.93}Cu_{0.07}O_7$ and $Dy_{1.99}Sr_{0.01}Sn_2O_7$ are characterized at the first stage by the metal analysis. The inductively coupled plasma spectroscopy (ICPES) and the energy dispersive X-ray analysis (EDS) are used to confirm the presence of metal species in the same cationic ratio as initially used and the observed compositions are summarized in Table 2. This suggests the stoichiometry in the compounds is perfectly maintained within the experimental errors (< 1 %). The EDS spectrum of these substituted pyrochlore oxide is shown in Fig. 3. Peaks in this spectrum show all cations present in each pyrochlores.

No other peaks are evident. Corresponding EDS spectrum of all substituted compounds indicates that the presence of the intended substituent's species within the lattice of each crystal examined.

The XRD Pattern of $Nd_{1.9}$ $Ho_{0.1}Zr_{1.8}Ce_{0.2}O_7$, $La_{1.95}Ce_{0.05}Zr_{0.29}Ce_{1.71}O_7$, $Y_{1.79}Pr_{0.21}Ru_{1.99}Pr_{0.01}O_7$, $Dy_{1.9}Yb_{0.1}Mn_{1.93}Cu_{0.07}O_7$ and $Dy_{1.9}Zr_{0.01}Sn_2O_7$, are shown in Fig.4. The XRD peaks are found to be broad and it is attributed to the nanocrystalline nature of all substituted pyrochlores. The X-ray pattern does not show any secondary phase. The respective hkl values are assigned to the peaks in the XRD are shown in Fig. 4 (a) to (e). In literature, the formation of either perovskite or pyrochlore structure was detected by the appearance of distinctive strong characteristic X-ray diffraction lines, especially those corresponding with reflections from the (222) planes in the pyrochlore structure and from (112) and (200) planes in the perovskite structure [51]. The presence of (222) reflections in the XRD spectrum for all substituted pyrochlores except $La_{1.95}Ce_{0.05}Zr_{0.29}Ce_{1.71}O_7$ sample confirmed the cubic pyrochlore structure [37, 52-56]. While, as seen from Fig. 4(b) for $La_{1.95}Ce_{0.05}Zr_{0.29}Ce_{1.71}O_7$ sample the XRD peaks with 2 theta θ values at 28.17 °, 32.18 °, 46.09°, 54.84°,
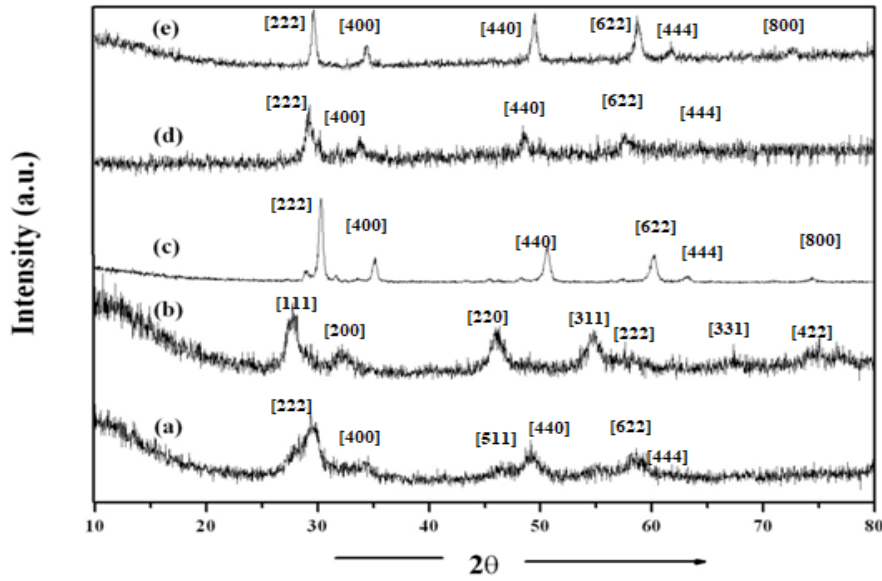
Fig. 4. X-ray diffraction patterns of substituted pyrochlore-type nanooxides.
(a) $Nd_{1.9}Ho_{0.1}Zr_{1.8}Ce_{0.2}O_7$, (b) $La_{1.95}Ce_{0.05}Zr_{0.29}Ce_{1.71}O_7$, (c) $Y_{1.79}Pr_{0.21}Ru_{1.99}Pr_{0.01}O_7$,
(d) $Dy_{1.9}Yb_{0.1}Mn_{1.93}Cu_{0.07}O_7$, (e) $Dy_{1.99}Sr_{0.01}Sn_2O_7$.

Table 3

X-ray diffraction data, particulate properties, TEM and infrared spectral data of substituted pyrochlore-type nanooxides

Substituted pyrochlore oxides	Radius ratio (r_A^{3+}/r_B^{4+})	Lattice constant 'a' nm	Mean crystallite size $\langle D \rangle$ x-Ray nm $\pm 10\%$	X-Ray density D_x (g.cm^{-3})	Apparent density D (g.cm^{-3})	Porosity $P=1-D/D_x$	Average grain size (from SEM) nm	Average grain size (from TEM) nm	Infrared spectral absorption band cm^{-1}	
									v_1	v_2
$Nd_{1.9}Ho_{0.1}Zr_{1.8}Ce_{0.2}O_7$	1.504	1.0496	28	6.969	1.247	0.821	23	20	592	423
$La_{1.95}Ce_{0.05}Zr_{0.29}Ce_{1.71}O_7$	1.367	0.5552	32	50.495	1.447	0.971	26	17	516	474
$Y_{1.79}Pr_{0.21}Ru_{1.99}Pr_{0.01}O_7$	1.661	1.0196	30	6.362	1.945	0.843	35	23	565	422
$Dy_{1.9}Yb_{0.1}Mn_{1.93}Cu_{0.07}O_7$	1.914	1.0454	22	6.429	1.945	0.698	28	14	559	407
$Dy_{1.99}Sr_{0.01}Sn_2O_7$	1.494	1.0415	37	7.894	2.098	0.734	35	30	631	427

57.33°,75.03° and 76.61° can be well indexed to (111), (200), (220), (311), (400), (331) and (422) planes of a cubic fluorite structure, respectively. These observed peaks are corresponded to the pure (undoped) $La_2Ce_2 O_7$ phase and are good agreement with literature [57, 58]. Further no more XRD peak corresponding to individual oxides was observed. This indicated the synthesized compounds do not contain any impurity phases and are pure pyrochlores of $A_2B_2O_7$ type.

There is an excellent agreement of the experimentally observed d-spacing values and relative intensities of substituted pyrochlores with the pure (undoped) respective pyrochlore oxides such as $Nd_2Zr_2O_7$, $La_2Ce_2 O_7$, $Y_2Ru_2O_7$, $Dy_2Mn_2O_7$ and $Dy_2Sn_2O_7$ [37, 52 - 58]. The lattice parameter 'a' is determined from the XRD pattern using the relation a = d $\sqrt{h^2 + k^2 + l^2}$, where d is the inter plane spacing of the diffraction peak and hkl denotes the Miller indices of the corresponding peak. The lattice parameter is given in Table 3, which is slightly less than the reported value [12, 52-58]. This can be due to the incorporation of dopants in to host lattice and also the nanocrystalline

nature of all substituted pyrochlores. It is well established phenomenon that the nanocrystalline system possesses high surface area and high chemical energy that make us slight distortion in the lattice and therefore lower lattice parameter [59] is obtained.

As it is known that, there is proximity in structure of defect fluorite and pyrochlore (A_2^{3+} B_2^{4+} O_7^{2-}) crystal structure and therefore differentiating one from the other is little different through XRD because it probes only a long range ordering. Therefore, the cation radii ratio (r_A^{3+} / r_B^{4+}) is complimenting the XRD analysis as the reported in literature [3, 4, 60]. The size between cations an A and B sites is supposed to be the driving force to stabilize the pyrochlore structure [61]. In the case of +3/+4 oxides, the ordered pyrochlore structure is favoured where cation ratio r_A / r_B is greater than 1.40. While for disordered fluorite structure is favourable at the cation radii ratio r_A / r_B between 1.20 to 1.40 [6, 62, 63]. The c -type structure can be implicit as a defect fluorite, if r_A / r_B is smaller than 1.17 [11, 64, 65]. However, these phase formation cannot be only depend on the relative radii of cations, but also depends on the sample processing condition [66].

Now let us analysed the structural investigation of the as – prepared substituted pyrochlore oxides were evaluated by cation radii ratio (r_A^{3+} / r_B^{4+}). Since the Shannon ionic radii of cation for eight coordinated A^{3+} and six coordinated B^{4+} was given [63] as: Nd^{3+} = 0.111 nm, Ho^{3+} = 0.102 nm, Zr^{4+} = 0.072nm, Ce^{4+} = 0.087 nm, La^{3+} = 0.116 nm, Ce^{3+} = 0.114 nm, Y^{3+} = 0.102 nm, Pr^{3+} = 0.113 nm, Ru^{4+} = 0.62 nm, Pr^{4+} = 0.085nm, Dy^{3+} = 0.103 nm, Yb^{3+} = 0.099 nm, Mn^{4+} = 0.053 nm, Cu^{2+} = 0.073 nm, Sr^{2+} = 0.126 nm and Sn^{4+} = 0.069 nm. As a result, the relative cation radii ratio (r_A^{3+} / r_B^{4+}) in all substituted pyrochlore oxide was between 1.494 to 1.914 except $La_{1.95}Ce_{0.05}Zr_{0.29}Ce_{1.71}O_7$ sample (see Table 3), which made these compounds adopt a stable pyrochlore structure and while the cation radius ratio (r_A^{3+}/r_B^{4+}) = 1.367 for $La_{1.95}Ce_{0.05}Zr_{0.29}Ce_{1.71}O_7$ compound showed a fluorite structure. These results were also consistent with the XRD pattern (see Fig. 4). Thus $La_{1.95}Ce_{0.05}Zr_{0.29}Ce_{1.71}O_7$ is a disordered fluorite structure which have relatively large amount of vacancy, while remaining substituted pyrochlores are ordered pyrochlore structure. However in the present investigation, the absence of the c – type super structure XRD pattern. Hence, it should be noted that the numerical value of cation radii ratio (r_A^{3+}/ r_B^{4+}) is used only as a broad guide line in view of some exceptions [66]. Thus, the deficiency of anions in the pyrochlore or fluorite type oxide facilitates the substitution of a wide range of cations on A and B sites leading to several composition with diverse properties such as electrical conductivity, dielectric and magnetic properties [67-69].

The particulate properties like X-ray density, apparent density, porosity and mean crystallite size of these substituted pyrochlore oxides are summarized in Table. 3. It is noticed that X-ray densities Dx are higher than the apparent density (D). This is attributed to the existence of the pores. The higher porosity corresponds with lower apparent density. These results were

explained on the basis that rare-earth ions have a bigger ionic radius as compared to other ions present in these pyrochlores.

The crystallite size $<D>_{X-ray}$ for all substituted pyrochlores are also calculated from the width of half maximum of three successive diffraction peaks using of Debye-Scherrer equation [70, 71]. $<D>_{X-ray}$ = 0.89.λ / β. Cos θ, where $<D>_{X-ray}$ is the average crystallite size , λ is the X-ray wavelength (0.15405 nm) θ is the diffraction angle and β is the full width of the half maxima of an observed XRD peak in radions (at a height half way between back ground and the peak maximum). The peak width (β) is inversely proportional to the crystallite size $<D>_{X-ray}$. This β can be measured with an accuracy $\pm$ 0.01° and it varies with 2θ as Cos θ. The observed XRD peak profile may contribute too many factors such as crystallite size, instrumental peak profile, microstrain of sample, solid solution inhomogeneity and temperature. The strongest 3 - 4 XRD peaks were used to calculate the average crystallite size $<D>_{X-ray}$ for all substituted pyrochlores. The observed average crystallite size is depicted in Table 3. These values are in the range of 22 nm to 37 nm (with an error of $\pm$ 10 %) for all substituted pyrochlores, indicating the nano size nature of compounds.

The morphologies of the synthesized substituted pyrochlores were studied using scanning electron micrographs (SEM) and which are depicted in Fig. 5. The observed SEM images for $Nd_{1.9}Ho_{0.1}Zr_{1.8}Ce_{0.2}O_7$, $La_{1.95}Ce_{0.05}Zr_{0.29}Ce_{1.71}O_7$ and $Dy_{1.99}Sr_{0.01}Sn_2O_7$ compounds reveals the grain in small and large platelets but the degree of agglomeration is high (Fig.5 (a), (b) and (e)). SEM images for $Y_{1.79}Pr_{0.21}Ru_{1.99}Pr_{0.01}O_7$ and $Dy_{1.9}Yb_{0.1}Mn_{1.93}Cu_{0.07}O_7$ shows the grain in irregular platelets with less aggregated (Fig.5 (c) and (d)). The average grain sizes of these substituted pyrochlores were found to be in the range 23 - 35 nm (Table 3).

Fig. 6 (a to e) exhibit the transmission electron micrographs (TEM) images of substituted pyrochlore compounds. The TEM images of all compounds except $Y_{1.79}Pr_{0.21}Ru_{1.99}Pr_{0.01}O_7$ revealed that the grains are plate like, nonaggregated and dense and some of the platelets have already been destroyed, while in the TEM image Fig. 6 (C) of $Y_{1.79}Pr_{0.21}Ru_{1.99}Pr_{0.01}O_7$ compound show the grain in spherical shape. The average grain sizes of these samples are found to be 14 to 30 nm (Table 3). The observed grain sizes determined from the TEM may be composed of many different crystallites. So the crystallite size determines from XRD (Scherrer equation) will never give exact grain size. Therefore, measuring grain or particle size can better and more efficiently be calculated via TEM than XRD. These average grain sizes (from TEM) confirm the formation of nano particles in the substituted pyrochlores.

To investigate the structural information of as-synthesized substituted pyrochlores, the selected area electron diffraction (SAED) was performed. The index of SAED pattern plane values is marked in Fig. 6 (a') to (e'). It is interesting to observe that the SAED pattern exhibit distinct lattice planes and these are in good agreement with the XRD pattern of substituted pyrochlores (see Fig. 4), which indicates that the sample
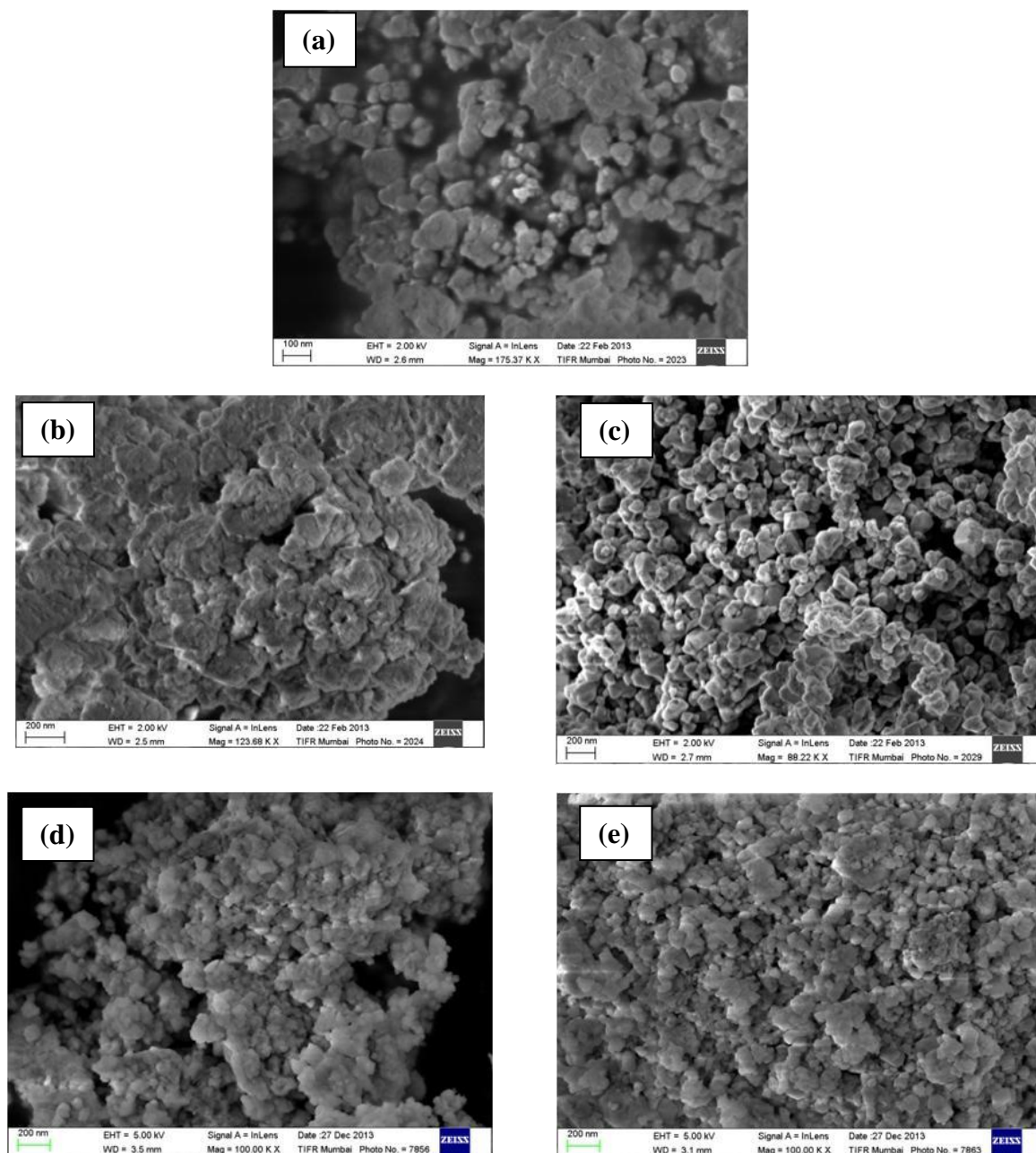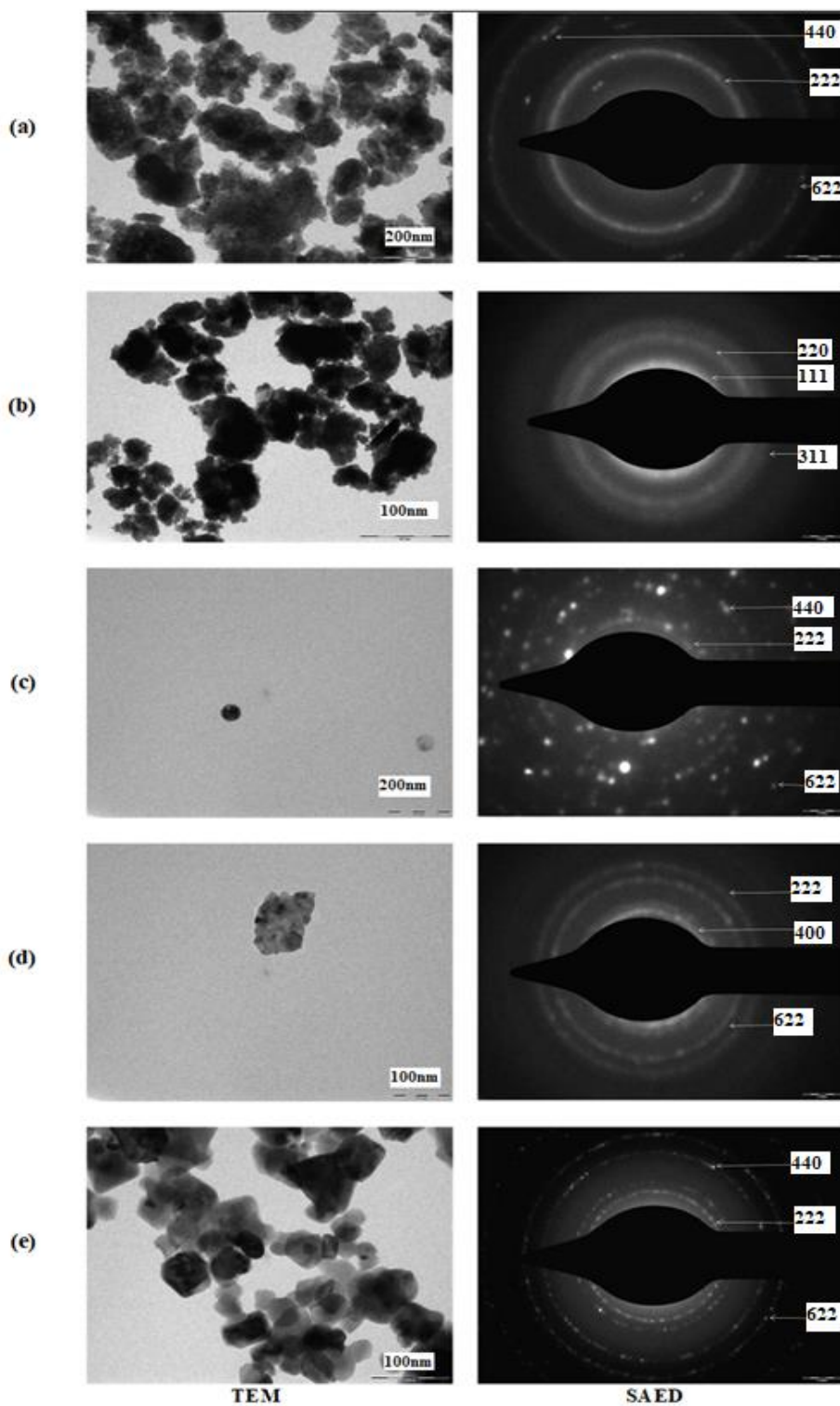
Fig. 5. Scanning electron micrographs (SEM) of substituted pyrochlore-type nanooxides. (a) $Nd_{1.9}Ho_{0.1}Zr_{1.8}Ce_{0.2}O_7$, (b) $La_{1.95}Ce_{0.05}Zr_{0.29}Ce_{1.71}O_7$, (c) $Y_{1.79}Pr_{0.21}Ru_{1.99}Pr_{0.01}O_7$, (d) $Dy_{1.9}Yb_{0.1}Mn_{1.93}Cu_{0.07}O_7$, (e) $Dy_{1.99}Sr_{0.01}Sn_2O_7$.

is of a single crystallographic phase. It is obvious that, the High Resolution Transmission Microscopy (HRTEM) of oxide reported in the literature [71] could indicate the presence of lattice distinct fringes. The lattice constant should be compared with respective undoped and doped oxides. But in the present study, we have synthesized only substituted pyrochlores. That's why we have not studied the HRTEM of these pyrochlores.

The IR spectra of the prepared substituted pyrochlore oxides recorded in a range of 1000 - 400 cm^{-1} are given in Table 3. The IR spectra are used to obtain the chemical bonding in such materials. For various pyrochlores, there is a difference in the distance for oxygen ion, A-site ion and B-site ion. All the substituted pyrochlores show a strong absorption band at around 540 - 631 (v_1) and 407 - 440 (v_2), which are

characteristics of pyrochlore structure [72, 73]. The band at around (v_1) is attributed to the M – O bridge (i.e. B - site bond of pyrochlore). The second band at around (v_2) is due to the bending vibration of the O–M–O bond (see Table 3). The observed absorption band v_1 and v_2 of the compounds would suggest that the Ln^{3+} ions (at A-site) and M^{4+} ions (Zr^{4+}etc ion at B-site) are sufficiently heavy to form quasi stationary identical framework, while the oxygen ions move in the potential wells formed by metal ions. Such charged distribution in the well (and hence the vibrational force constant) depends on the effective interatomic distance, which varies with substituent's ion at the A-site or the valency of M–O bond at B-site of pyrochlores. The peak frequencies appear v_1 or v_2, which depend on the ionic radius rather than on the atomic mass of A-site or B-site cations.

Fig. 6. Transmission electron micrographs (TEM) and SAED pattern of substituted pyrochlore-type nanooxides.
(a) $Nd_{1.9}Ho_{0.1}Zr_{1.8}Ce_{0.2}O_7$, (b) $La_{1.95}Ce_{0.05}Zr_{0.29}Ce_{1.71}O_7$, (c) $Y_{1.79}Pr_{0.21}Ru_{1.99}Pr_{0.01}O_7$,
(d) $Dy_{1.9}Yb_{0.1}Mn_{1.93}Cu_{0.07}O_7$, (e) $Dy_{1.99}Sr_{0.01}Sn_2O_7$.

2.2.2. Electrical conductivity studies

The variation of electrical conductivity (log σ) against temperature (1/T) for $Nd_{1.9}Ho_{0.1}Zr_{1.8}Ce_{0.2}O_7$, $La_{1.95}Ce_{0.05}Zr_{0.29}Ce_{1.71}O_7$, $Y_{1.79}Pr_{0.21}Ru_{1.99}Pr_{0.01}O_7$, $Dy_{1.9}Yb_{0.1}Mn_{1.93}Cu_{0.07}O_7$ and $Dy_{1.99}Sr_{0.01}Sn_2O_7$ compounds are shown in Fig. 7. It is obvious that the conductivity of these compounds increases with temperature according to the relation $\sigma = \sigma_o \, Exp^{\,(-Ea/KT)}$ where Ea is the activation energy, σ_o is the independent constant, K is Boltzmann constant and T is the absolute temperature [74]. The electrical conductivity experiments for these pyrochlores are repeated three times and the results are found to be reproducible. The plot of log σ Vs T^{-1} shows the initial decrease in electrical conductivity in the temperature range of 301 to 400 K, which corresponds to the desorption of the adsorbed water
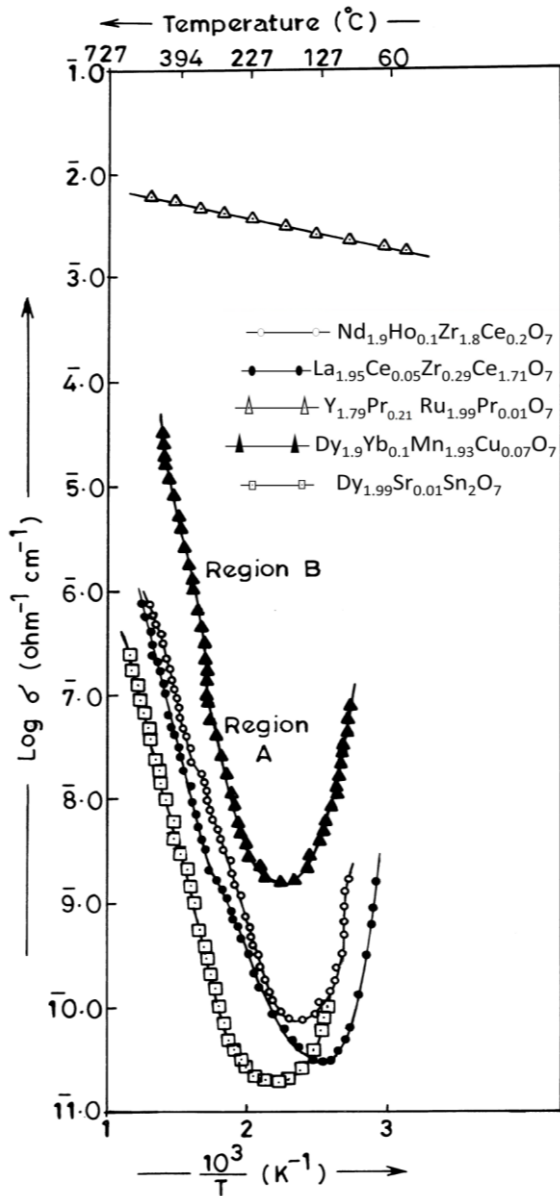
Fig. 7. Plot of log σ against T^{-1} of substituted pyrochlore-type nanooxides.

Fig. 8. Plot of thermoelectric power, μ (volt K^{-1}) against temperature, T (K) of substituted pyrochlore-type nanooxides.

molecules on the particle surface. The conductivity then increases linearly with increasing temperature. All above compounds, except $Y_{1.79}Pr_{0.21}Ru_{1.99}Pr_{0.01}O_7$ and $Dy_{1.99}Sr_{0.01}Sn_2O_7$ temperature variation of the conductivity exhibit two distinct slopes with a 'break' in the slope between them. The temperature at which the break occurs was found to be about ~ 610 K (Table 4) and this discontinuity can be attributed to a strong exchange interaction between the outer and inner electrons. The activation energy (E_a) in eV has been calculated using the above relation and is tabulated in Table 4. The values of Ea in region A are lower than those in the region B. The lattice defect (i.e. substituent's) conduction is favored below 610 K (Region A), while a thermally activated mobility of charge carriers at a higher temperature above 610 K (Region B). Hence, the electrical conduction in the system under investigation is due to the electron acceptor hopping in the sublattices between $Ce^{3+} \leftrightarrow Ce^{4+}$ or $Mn^{3+} \leftrightarrow Mn^{4+}$ ions and results increasing in activation energy in the region B.

The small activation energy (Ea) was observed for $Y_{1.79}Pr_{0.21}Ru_{1.99}Pr_{0.01}O_7$ pyrochlore, which probably corresponds to oxygen nonstoichiometry and the valence stabilities of ruthenium (Ru^{4+}) being able to change its valence far more easily because of the stable Yttrium element [75]. The electrical conduction will be an 'inductive' effect, where the size of rare earth ions (Ln^{3+}) competes with the Ru^{4+} ions and withdraws electron density from the Ru - O_π bonding network. The magnitude of the inductive effect increases for a smaller size of Y^{3+} pyrochlore, which leads to a more semiconducting character for this synthesized compound. It is also known that the electrical conductivity is strongly affected by both (i) the cation radius ratio and (ii) unit cell volume. Thus, the electrical conductivity was observed in the vicinity of the crystal phase boundary in the pyrochlore oxides [76, 77].

The thermoelectric power measurements for substituted pyrochlore oxides are illustrated in Fig. 8. The sign of thermoelectric power is positive for all samples except $Y_{1.79}Pr_{0.21}Ru_{1.99}Pr_{0.01}O_7$ sample. All compounds of pyrochlore show a very steep decrease of

Table 4

Electrical conductivity data and dielectric properties of substituted pyrochlore-type nanooxides

Substituted pyrochlore oxides	Temperature corresponding to desorption of adsorbed water (K)	Conductivity measurements				Hall effect measurements at room temperature				
		Region	Temp.range (K)	Activation energy Ea (eV)	Break temp. (transition temperature) T_c (K)	Current passed (nA)	Specific Resistivity at room temp. Ohm cm	Types of charge carriers	Average Hall coefficient cm^3/C	Mobility cm^2/Vs
$Nd_{1.9}Ho_{0.1}Zr_{1.8}Ce_{0.2}O_7$	400	A	302.5-610	0.823	610	100	1.308×10^5	p-type	2.212×10^7	169.1
		B	610-805	1.157						
$La_{1.95}Ce_{0.05}Zr_{0.29}Ce_{1.71}O_7$	378	A	302.5-587.5	0.598	587.5	100	4.897×10^{10}	p-type	2.679×10^7	5.471×10^{-4}
		B	587.5-805	1.085						
$Y_{1.79}Pr_{0.21}Ru_{1.99}Pr_{0.01}O_7$	-	-	302.5-610	0.055	--	100	1.238	n-type	-9.963×10^2	805.0
$Dy_{1.9}Yb_{0.1}Mn_{1.93}Cu_{0.07}O_7$	398.5	A	302.5-585	1.008	585	20	1.642×10^7	p-type	8.831×10^8	56.01
		B	585-805	1.241						
$Dy_{1.99}Sr_{0.01}Sn_2O_7$	409	A	302.5-805	1.042	--	20	6.172×10^6	p-type	1.133×10^8	18.35

the positive thermoelectric power from 300 to 480 K and then turn to negative and its magnitude increases from 500 to 700 K. The first phenomenon must be attributed to a decrease in the concentration of interstitial oxygen ions, which confirms that oxygen vacancies must be ionic charge carriers. Then the thermoelectric power is negative even above 500 K and it increases slowly due to electronic type defects.

For $Y_{1.79}Pr_{0.21}Ru_{1.99}Pr_{0.01}O_7$ show a very steep decrease of negative thermoelectric power from room temperature 300 to 625 K. The cubic pyrochlore structure of this compound has a narrow Ru: 4d (t_{2g}) band at the Fermi energy, which enhances the electron – electron interaction or the charge carriers are localized on the defect centers. Hence this compound is n-type semiconductivity.

We have also measured the Hall effect constants in the magnetic field of 0.54 T at room temperature after passing current in nano ampere through the samples. The results are listed in Table 4. All substituted pyrochlores show p-type semiconductivity except $Y_{1.79}Pr_{0.21}Ru_{1.99}Pr_{0.01}O_7$ and which has n-type semiconductivity. The observed variation of specific resistivity is due to different semiconducting properties of substituted pyrochlores and it is also reflected in the mobility (see Table 4). Normally the increase in specific resistivity is attributed to the reduction in mobility of the charge carrier. The low value specific resistivity and high value of mobility in $Y_{1.79}Pr_{0.21}Ru_{1.99}Pr_{0.01}O_7$ are due to the decrease in B-site hopping length of this sample. The average Hall coefficient at room temperature for all substituted pyrochlores except $Y_{1.79}Pr_{0.21}Ru_{1.99}Pr_{0.01}O_7$ is positive indicating holes are majority carriers.

2.2.3. Dielectric studies

The dielectric constant (ε') and dielectric loss (tan δ) against frequency in the range 1 - 600 kHz were recorded at room temperature for $Nd_{1.9}Ho_{0.1}Zr_{1.8}Ce_{0.2}O_7$, $La_{1.95}Ce_{0.05}Zr_{0.29}Ce_{1.71}O_7$, $Y_{1.79}Pr_{0.21}Ru_{1.99}Pr_{0.01}O_7$, $Dy_{1.9}Yb_{0.1}Mn_{1.93}Cu_{0.07}O_7$ and $Dy_{1.99}Sr_{0.01}Sn_2O_7$ compounds. The representative of dielectric constant (ε') and dielectric loss (tan δ) versus the frequencies of $Nd_{1.9}Ho_{0.1}Zr_{1.8}Ce_{0.2}O_7$ is shown in Fig.9 (a) and (b). The value of dielectric constant (ε') is high at low frequencies, it decreases up to 130 kHz and then remains constant up to 6 MHz (see Fig. 9(a)). This is due to inequality of charge distribution at grain boundaries, which leads to non-uniform conductivity by interfacial and dipolar polarizations up to 130 kHz and beyond this domain wall motion occurs. In the higher frequencies range; the dielectric constant would be saturated because the electronic exchange cannot follow the a. c. field beyond certain critical frequencies.

Similarly, the large values of dielectric loss (tan δ) at lower frequencies for these substituted pyrochlores (Fig. 9(b)) are due to the predominance of the oxygen vacancies, grain boundary defect etc.[78, 79]. The decrease in dielectric loss (tan δ) is the fact that any species contributing to polarisability is bound to show lagging behind at higher frequencies. Thus, the polarization, as well as increased conductivity and activation energy (Ea) are affecting the dielectric constant (ε') and dielectric loss (tan δ). The local magnetic ordering can also induce non-centrosymmetry and weak polarization at high frequencies in these substituted pyrochlore oxides.

(a)   (b)
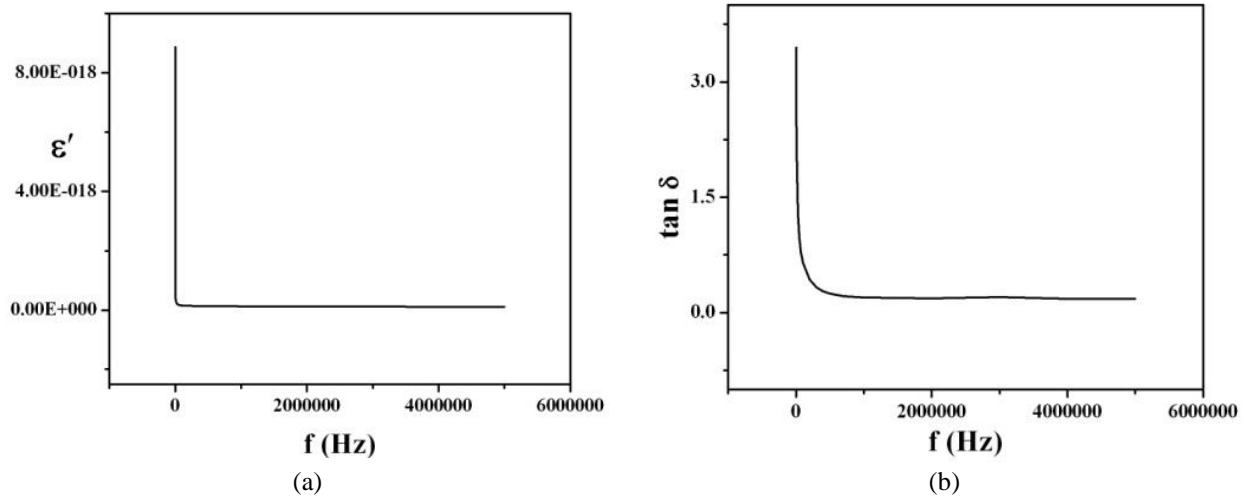
Fig. 9. Plot of (a) variation of dielectric constant (ε') with frequency and (b) dielectric loss (tan δ) with frequency for Substituted pyrochlore, $Nd_{1.9}Ho_{0.1}Zr_{1.8}Ce_{0.2}O_7$ compound.

2.2.4. Magnetic studies
2.2.4.1 $Nd_{1.9}Ho_{0.1}Zr_{1.8}Ce_{0.2}O_7$

Magnetization (M) against the applied field (H) of $Nd_{1.9}Ho_{0.1}Zr_{1.8}Ce_{0.2}O_7$ was performed to investigate the magnetic activity of synthesized substituted pyrochlore nanooxides (Fig. 10 (a)). In our experimental observation, with a slight kink around the origin, we have obtained a room temperature hysteresis loop, suggesting small but definite ferromagnetic ordering along with appropriate paramagnetic and super paramagnetic components. Zirconium ions (Zr^{4+}), which do not lead to ferromagnetism at room temperature, are available in the sample. There are, however, some isolated rare earth ions (Ln^{3+}) that contribute to RT ferromagnetism. It is fair to assume that most of the paramagnetic components are induced by the spin of these isolated Ln^{3+} ions at RT. Furthermore, because the particle size is in the nano region, some of the particles may be superparamagnetic and the two contributions (paramagnetism and superparamagnetism) at room temperature will complicate the magnetic activity.

If we carefully see from Fig. 10(a) that ferromagnetic activity within clusters is shown at low-field hysteresis (say 0 to 5000 Oe) and high-field paramagnetic behaviour above 20000 Oe is shown. The linear paramagnetic behaviour has been adapted to a straight line with an interception (about 0.16 emu g^{-1}). For positive and negative field regions, since the intercepts are similar, then paramagnetic behaviour is verified. Synthesized nano sized materials form superparamagnetic clusters (20 nm from TEM see Table 3). Therefore, the ferromagnetic activity of this compound is responsible for central low field hysteresis. Similar coexistence of ferromagnetic and paramagnetic moment has proposed that, the uncontrolled formation of lattice defects can generate carriers (i.e. disorder effect) or the interaction between bound magnetic polarons that results in ferromagnetic ordering [80, 81].
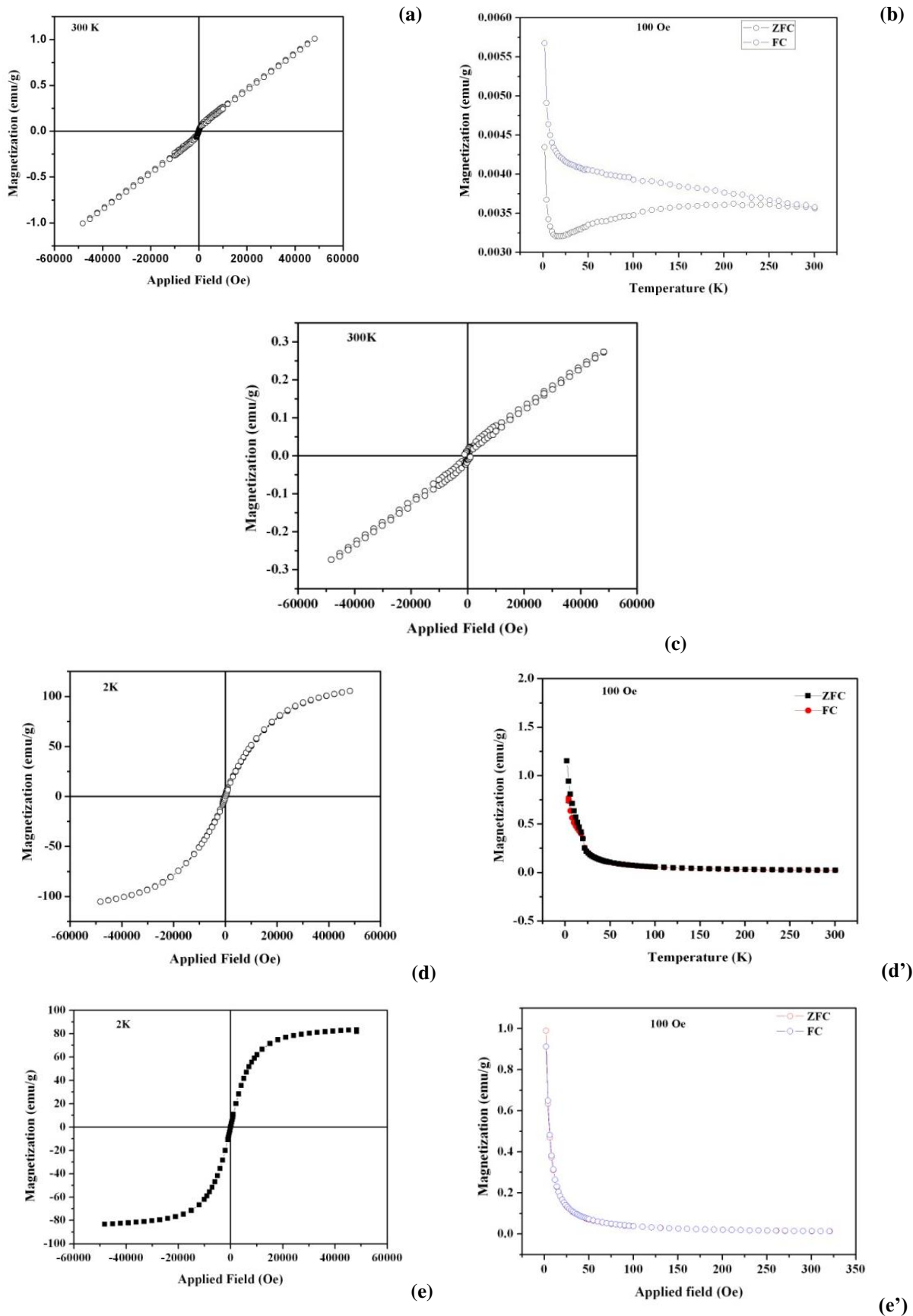
2.2.4.2. For $La_{1.95}Ce_{0.05}Zr_{0.29}Ce_{1.71}O_7$

Zero-field-cooled (ZFC) and field-cooled (FC) measurements investigate low temperature behaviour. Fig. 10(b) shows the $La_{1.95}Ce_{0.05}Zr_{0.29}Ce_{1.71}O_7$ sample

ZFC-FC curve obtained using the (SQUID) magnetometer in the temperature range 5 to 325 K. In the absence of a magnetic field, the ZFC curve is obtained by initially cooling the sample from 325 to 5 K and heating it in an applied magnetic field 100 Oe while magnetization is recorded. The sample is cooled in the same field for FC measurements and magnetization is registered during heating-up. The Curie transition temperature (T_c) of the $La_{1.95}Ce_{0.05}Zr_{0.29}Ce_{1.71}O_7$ sample has been found to be above 300 K. By removing para and diamagnetic contribution, the difference between ZFC and FC gives the net magnetization value ($\Delta M = FC - ZFC$) corresponding to ferromagnetic contribution in the sample [82]. The difference between ZFC and FC in the present sample is highest above room temperature (i.e. 325 K). This also indicates that the sample contains stronger ferromagnetic interactions. The ferromagnetism observed can occur for different reasons.

In a synthesized nanosized sample, through XRD and SAED studies, we have not found any sign of secondary phases. It rules out the possibility of some other impurity phase in the sample being present. In literature, a theory of acceptor defect-mediated ferromagnetism was developed [83]. The acceptor defect (p-type) carriers among which Ce vacancies (i.e. disorder effect) mediate the parallel alignment of magnetic moments that show ferromagnetism at room temperature are also shown in our sample.

2.2.4.3. For $Y_{1.79}Pr_{0.21}Ru_{1.99}Pr_{0.01}O_7$

The magnetizations versus applied field (M-H) curves recorded by VSM of $Y_{1.79}Pr_{0.21}Ru_{1.99}Pr_{0.01}O_7$ at 300 K are shown in Fig. 10(c). Magnetic dilution with yttrium (Y) is found to induce a decrease in the magnetic moment of the compounds, while substituent with Pr at Y sites increase the magnetic moment. This is shown since the magnetic order of the sample can be tuned by adjusting the ferromagnetic order by adding Pr, which is often correlated with the long-range magnetic ordering of Ru^{4+} ions. It is therefore probable that the magnetic response of the site Ru^{4+} is masked by the high response of Pr^{3+} ions in the substituted pyrochlore. We emphasize that it is important to include the contribution of both the

366

Fig. 10. Magnetization Vs Applied field and ZFC and FC magnetization Vs temperature of substituted pyrochlore-type nanooxides. (a) $Nd_{1.9}Ho_{0.1}Zr_{1.8}Ce_{0.2}O_7$, (b) $La_{1.95}Ce_{0.05}Zr_{0.29}Ce_{1.71}O_7$, (c) $Y_{1.79}Pr_{0.21}Ru_{1.99}Pr_{0.01}O_7$, (d) and (d') $Dy_{1.9}Yb_{0.1}Mn_{1.93}Cu_{0.07}O_7$, (e) and (e') $Dy_{1.99}Sr_{0.01}Sn_2O_7$.

magnetic sites of Pr and Ru to achieve a reasonable agreement between the experimental and theoretical magnetic moment values. Thus, considering the orbital and spin contribution to the total magnetic moment $2(J(J+1))^{1/2}$ for Pr^{3+} ions, magnetic moments (μ) were evaluated, where for Ru^{4+} ions we consider only the spin contribution $2(S(S+1))^{1/2}$ in a low spin with $S = 1$ [84]. The concordance between the value of the experimental and theoretical magnetic moment (μ) suggests that the contribution of both magnetic sites results in the magnetic response of the studied sample. This sample is, therefore, weakly ferromagnetic.

2.2.4.4. For $Dy_{1.9}Yb_{0.1}Mn_{1.93}Cu_{0.07}O_7$

No magnetic hysteresis for the $Dy_{1.9}Yb_{0.1}Mn_{1.93}Cu_{0.07}O_7$ sample was observed at 300 K. The magnetic hysteresis is observed when the temperature is reduced to 2.0 K, (Fig. 10(d)). A clear hysteresis showing the ferromagnetic aspect of the sample has been observed. It should be noted that even after a magnetic field of 60000 Oe was applied, the magnetization value did not show saturation. This indicates magnetic relaxation in the sample. The nanosize particles present in the current sample undergoing supermagnetism relaxation at room temperature (14 nm from TEM, see Table 3) may be the explanation for not obtaining a saturated magnetization value.

We have now analyzed the magnetic properties of this sample (i.e. $Dy_{1.9}Yb_{0.1}Mn_{1.93}Cu_{0.07}O_7$) using the SQUID magnetometer in the temperature range 2 - 325 K. Now let us verify if the supermagnetism is present or not in our sample. The magnetization dependence on temperature is shown in Fig. 10(d'). The figure shows a plot of ZFC and FC magnetization measurements performed on the material by applying a 100 Oe field. The difference between ZFC and FC is negligible, i.e. reversible, and the curve mostly follows Curie-Weiss paramagnetic behaviour in this sample. The ferromagnetic transition of this sample was observed at $Tc = 50 \pm 1$ K. Net magnetization, particularly for this sample, does not become zero until about 325 K. This also provides strong proof that ferromagnetism in the sample is observed at 325 K. We, therefore, infer that both the Mn and Ln sublattices are ferromagnetism and approach saturation in strong magnetic fields; the Ln^{3+} - Mn^{4+} spin - spin interactions of ferromagnetism suppress the frustrated antiferromagnetic component on the Mn^{4+} ion array that is manifested at the lower field in $Dy_{1.9}Yb_{0.1}Mn_{1.93}Cu_{0.07}O_7$. At low temperatures, the manganese pyrochlore is ferromagnetic; the fact is well explained by dominant ferromagnetism for Mn - O - Mn bond angle of about 130°. This bond angle in the manganese pyrochlore structure is not susceptible to the size of rare earth (RE^{3+}) ions [85, 86].

2.2.4.5. For $Dy_{1.99}Sr_{0.01}Sn_2O_7$

The magnetization (M) versus magnetic field (H) measured at 2 K for $Dy_{1.99}Sr_{0.01}Sn_2O_7$ was seen in Fig. 10 (e). A clear hysteresis loop is observed in this sample. In addition, the temperature (T) dependent magnetization (M) curve of this sample was recorded using the SQUID magnetometer in the 5 - 325 K temperature range (see

Fig.10 (e')). By applying a magnetic field at 100 Oe, the ZFC and FC (M - T) curves were measured. The difference between ZFC and FC gives a net magnetization value in the sample, which gives antiferromagnetic regime in a sample. The difference is insignificant for this sample and the curves show Curie-Weiss paramagnetic behaviour. It should be noted that the steep increase in magnetization seems to be intrinsic to diluted magnetic oxide at low temperatures (~ 35 K) and indicates the presence of paramagnetic phase at low temperatures.

In the present sample ($Dy_{1.99}Sr_{0.01}Sn_2O_7$), in which the Sn^{4+} ion is non magnetic and Dy^{3+} ions are chosen to be magnetic. When Sr^{2+} is substituted for Dy^{3+}, its large size and lower charge enable it to compete more strongly for oxygen electrons. At the same time, the Sn^{4+}- O interaction is reduced and the structure of the disorder is formed at the A - site of the pyrochlore [81]. Therefore, the formation of lattice defect can generate carriers that mediate ferromagnetic ordering in this sample.

Conclusions

a) X-ray diffraction and SAED pattern for all substituted pyrochlores have indicated the formation of single-phase pyrochlore with a cubic structure except for the $La_{1.95}Ce_{0.05}Zr_{0.29}Ce_{1.71}O_7$ sample, which shows fluorite structure. TEM micrographs of these pyrochlore systems are found to be the average grain size 14 to 30 nm, indicate all are nanosized materials.

b) The temperature dependence of the electrical conductivity of these substituted pyrochlores exhibits two different slopes with a 'break'. A strong exchange interaction between the outer and the inner electron can be attributed to this discontinuity. Measurements of thermoelectric power and Hall effect showed p-type semiconductivity for all compounds except for $Y_{1.79}Pr_{0.21}Ru_{1.99}Pr_{0.01}O_7$, and this showed n-type semiconductivity, indicating that Ru^{4+} ions are trapped by the carriers. Interfacial polarization followed by domain wall motion (i.e. the Maxwell – Wagner model) observed in dielectric constant and dielectric loss analysis.

c) Magnetic properties of substituted pyrochlores such as $Nd_{1.9}Ho_{0.1}Zr_{1.8}Ce_{0.2}O_7$, $Y_{1.79}Pr_{0.21}Ru_{1.99}Pr_{0.01}O_7$, and $Dy_{1.9}Yb_{0.1}Mn_{1.93}Cu_{0.07}O_7$, showed a hysteresis loop due to small but definite ferromagnetic ordering along with essential paramagnetic and superparamagnetic components. For the antiferromagnetic to paramagnetic transition, ZFC and FC magnetization measurements for $La_{1.95}Ce_{0.05}Zr_{0.29}Ce_{1.71}O_7$ and $Dy_{1.99}Sr_{0.01}Sn_2O_7$ compounds showed a Curie-Weiss activity at temperature Tc.

d)

Khanvilkar M.B. - M. Sc. Ph. D, Associate Professor;
Nikumbh A.K. - M.Sc. Ph. D, Professor;
Patange S.M. - M.Sc. Ph. D, Associate Professor;
Pawar R.A. - M.Sc. Ph. D, Professor;
Karale N.J. - M.Sc. Ph. D, Assistant Professor;

Nighot D.V. - M.Sc. Ph. D, Associate Professor;
Nagwade P.A. - M.Sc. Ph. D, Assistant Professor;
Sangale M.D. - M.Sc. Ph. D, Associate Professor;
Gugale G.S. - M.Sc. Ph. D, Associate Professor.

[1]   J.E. Greedan, J. Mater. Chem. 11, 37 (2001); https://doi.org/10.1039/B003682J.
[2]   M.A. Subramanian, A.W. Sleight, Handbook on the Physics and Chemistry of Rare Earth 16, 225 (1993).
[3]   F. Brisse and O. Knop, Canadian. J. Chem. 45, 609 (1967); https://doi.org/10.1139/v67-101.
[4]   K.R. Whittle, L.M.D. Cranswick, S.A.T. Redfern, I.P. Swainson and G.R. Lumpkin, S. Solid State Chem. 182, 442 (2009); https://doi.org/10.1016/j.jssc.2008.11.008.
[5]   M. Pirzda, R. W. Grimes and L. Minervini, Solid State Ionics 140, 201 (2001); https://doi.org/10.1016/S0167-2738(00)00836-5.
[6]   E. Reymolds, P.E.R. Blamshard, Q. Zhou and B.J. Kennady. Phys. Rev. B. 85, 132101 (2012); https://doi.org/10.1103/PhysRevB.85.132101.
[7]   J. Lian, J. Chen, L. M. Wang, R. C. Ewing, J. M. Farmer, L. A. Boatner and K. B. Helean, Phys. Rev. B 68, 134107 (2003); https://doi.org/10.1103/PhysRevB.68.134107.
[8]   B.P. Mandal, P.S.R. Krishna and A.K. Tyagi, J. Solid State Chem. 183, 41 (2010); https://doi.org/10.1016/j.jssc.2009.10.010.
[9]   J.B. Goodenough and R.N. Castellano, J. Solid State Chem. 44, 108 (1982); https://doi.org/10.1016/0022-4596(82)90406-6.
[10] M. Fathi Dehkharghani, M.R. Rahimipour and M. Zaheri, Surface and coatings Technology 399, 126174 (2020); https://doi.org/10.1016/j.surfcoat.2020.126174.
[11] M. Malathi, K.Sreenu, G. Ravi, P. Vijaya kumar, C.S. Reddy, R. Guje, R. Velchuri and M. Vithal. J. Chem. Sci. 129(8), 1193 (2017); https://doi.org/10.1007/s12039-017-1321-3.
[12] S. Khademinia, M. Behzad, Intr. Nano. Lett. 5, 101 (2015); https://doi.org/10.1007/s40089-015-0143-x.
[13] S.V. Wang, B.D. Begg and L.M. Wang, J. Mater. Res. 14(12), 4470 (1999); https://doi.org/10.1557/JMR.1999.0606.
[14] N. Sharma, G.V. Subbarao and B.V.R. Chowdari, J. Power Sources 159, 340 (2006); https://doi.org/10.1016/j.jpowsour.2006.04.050.
[15] D. Jin, X. Yu and H. Yang, J. Alloy. Com. 474(1-2), 557 (2009); https://doi.org/10.1016/j.jallcom.2008.06.159.
[16] J. Wu, X.Z. Wei, N.P. Padture, P.G. Klements, M. Gell, E. Garcia, P. Miranzo and M.I. Osendi, J. Am. Ceram. Soc. 85, 3031 (2002); https://doi.org/10.1111/j.1151-2916.2002.tb00574.x.
[17] L. Minervini and R.W. Grimes, J. Am. Ceram. Soc. 83(8), 1873 (2000); https://doi.org/10.1111/j.1151-2916.2000.tb01484.x.
[18] M.P. Van Dijk, K.J. De Vries and A.J. Burggraaf, Solid State Ionics 9(10), 913 (1983); https://doi.org/10.1016/0167-2738(83)90110-8.
[19] M.R. Winter and D.R. Clarke, J. Am. Ceram. Soc. 90(2), 533 (2007); https://doi.org/10.1111/j.1551-2916.2006.01410.x.
[20] F.W. Poulsen, M. Glerup and P. Holtappels, Solid State Ionics 135, 595 (2000); https://doi.org/10.1016/S0167-2738(00)00417-3.
[21] K. Chitrarasu, S. Amirthapadia, P. Jegadesan and P. Thangadurai, Mater.Lett. 289, 4 (2018.
[22] J.M. Longo, P.M. Raccah and J.B. Goodenough, Mater. Res. Bull. 4, 191 (1969); https://doi.org/10.1016/0025-5408(69)90056-7.
[23] R. Kanno, Y. Takeda, T. Yamanoto, Y. Kawamoto and O. Yamamoto, J. Solid State Chem. 102, 106 (1993); https://doi.org/10.1006/jssc.1993.1012.
[24] M. Field, B.J. Kennedy and B.A. Hunter, J. Solid State Chem. 151, 25 (2000); https://doi.org/10.1006/jssc.1999.8608.
[25] N. Taira, M. Wakeshima and Y. Hinatsu, J. Solid State Chem. 144, 216 (1999); https://doi.org/10.1006/jssc.1998.8113.
[26] M.D.R. Marques, F.S. Portela, A.A.M. Oliveira, P. Barrozo, N.O. Moreno, P.C.A. Brito and J.A. Aquiar, Physica B 407, 3106 (2012); https://doi.org/10.1016/j.physb.2011.12.037.
[27] C. Abate, V. Esposito, K. Duncan, J.C. Nino, D.M. Gattia, E.D. Wachsman and E. Traversa, J. Am. Ceram. Soc. 93(7), 1970 (2010); https://doi.org/10.1111/j.1551-2916.2010.03666.x.
[28] N. Taira, M. Wakeshima and Y. Hinatsu, J. Mater. Chem. 12, 148 (2002); https://doi.org/10.1039/B105179M.
[29] Q. Cui, N.N. Wang, N. Su, Y.Q. Cui, B.S. Wang, T. Shinmi, T. Irifune, J.A. Alonso and J.G. Cheng, J. Magn. Magn.Mater.490, 165494 (2019); https://doi.org/10.1016/j.jmmm.2019.165494.
[30] J.E. Greedan, N.P. Raju and M.A. Subramanian, Solid State Commun. 99, 399 (1996); https://doi.org/10.1016/0038-1098(96)00295-5.
[31] J. Snyder, J.S. Slusky, R.J. Cava and P. Schiffer, Nature (London) 413, 48 (2001); https://doi.org/10.1038/35092516.
[32] Satoshi Iikubo, Shunsuke Yoshii, Taketomo Kageyama, Keisuke Oda, Yasuyuki Kondo, Kazuhiro Murata1 and Masatoshi Sato, J. Phys. Soc. Japan 70, 212 (2001); https://doi.org/10.1143/JPSJ.70.212.
[33] M. Sato, and J.E. Greedan, J. Solid State Chem. 67, 248 (1987); https://doi.org/10.1016/0022-4596(87)90360-4.

[34] N. Imamura, M. Karppinen, H. Yamauchi and J.B. Goodenough, Phys. Rev. B 82, 132407 (2010); https://doi.org/10.1103/PhysRevB.82.132407.

[35] K. Chitrarasu, S. Jayabalan, S. Amirthapandian and P. Thangadurai, Solid State Science 105, 106245 (2020); https://doi.org/10.1016/j.solidstatesciences.2020.106245.

[36] K. Matsuhira, Y. Hinatsu, K. Tenya, H. Amitsuka and T. Sakakibara, J. Phys. Soc. Japan 71(6), 1576 (2002); https://doi.org/10.1143/JPSJ.71.1576.

[37] F. Brisse and O. Knop Can. J. chem. 46, 859 (1968); https://doi.org/10.1139/v68-148.

[38] X. Gong, P. Wu, W. Chen and H. Yang, J. Mater. Res. 13(2), 469 (1998); https://doi.org/10.1557/JMR.1998.0061.

[39] H. Kumar, and A.K. Pramanik, J. Phys. Chem. C. 123(20), 13036 (2019); https://doi.org/10.1021/acs.jpcc.9b02011.

[40] D. Pesin and L. Balents, Nature Physics. 6, 376 (2010); https://doi.org/10.1038/nphys1606.

[41] S. Zhu, H. Liu, J. Bian, Y. Feng and Q. Sun, J. Philosophical Magazine 100, 126 (2020); https://doi.org/10.1080/14786435.2019.1667546.

[42] G. Giampoli, J. Li, A.P. Ramirez and M. Subramanian, Inorg. Chem 56, 4706 (2017); https://doi.org/10.1021/acs.inorgchem.7b00345.

[43] J.A. Labrincha, J.R. Frade and F.M.B. Marques, J. Mater. Sci. 28, 3809 (1993); https://doi.org/10.1007/BF00353183.

[44] R. Vassen, X.G. Cao, F. Tietz, D. Basu and D. Stover, J. Am. Ceram. Soc. 83, 2023 (2000); https://doi.org/10.1111/j.1151-2916.2000.tb01506.x.

[45] K. Bhattacharya, A. Hartridge, K.K. Malick and J.L. Woodhead, J. Mater. Sci. 29, 6076 (1994); https://doi.org/10.1007/BF00354544.

[46] Z. Wang, G. Zhou, D. Jiang, and S. Wang, J. Advanced Ceramics. 7(4), 289 (2018); https://doi.org/10.1007/s40145-018-0287-z.

[47] Y. Matsumura, M. Yoshinaka, K. Hirota and O. Yamaguchi, Solid State Commun. 104, 341 (1997); https://doi.org/10.1016/S0038-1098(97)00332-3.

[48] M.B. Khanvilkar, A.K. Nikumbh, R.A. Pawar, N.J. Karale, D.V. Nighot and, G.S. Gugale, J. Mater. Sci. in Electronics 30, 13217 (2019); https://doi.org/10.1007/s10854-019-01685-3.

[49] K. Nakamoto, Infrared spectra of Inorganic and coordination compounds (Wiley-Interscience , New York, 2nd Edn. 1970.

[50] J.A. Allan, N.D. Baird and A.L. Kassyk, J. Therm.Anal. 16, 79 (1979); https://doi.org/10.1007/BF01909635.

[51] T.V an Dijk, K.J. de Vries and A.J. Burggraof, Physica Status Solid A 58, 115 (1980); https://doi.org/10.1002/pssa.2210580114.

[52] L. Kong, I. Karatchevtseva, D.J. Gregg, M.G. Blackford, R. Holmes, G. Triani. J. European Ceram. Soc. 33, 3273 (2013) And JCPDS File No. 781623 (https://doi.org/10.1016/j.jeurceramsoc.2013.05.011.

[53] J. Kim, P.C. Shih, K.C. Tsao, Y.T. Pan, X. Yin, C.J. Sun and H. Yang. J. Am. Chem. Soc. 139, 12076 (2017) And JCPDS File No. 830637 (https://doi.org/10.1021/jacs.7b06808.

[54] N. Imamura, M. Karppinen, and H. Yamauchi, Solid State Commun. 144(3-4), 98 (2007); https://doi.org/10.1016/j.ssc.2007.08.015.

[55] Q. Cui, N.N. Wang, N. Su, Y.Q. Cui, B.S. Wang, T. Shinmei, T. Trifune, J.A. Atonso and J.G. Cheng, J. Magn. Magn. Mater. 490, 165494 (2019); https://doi.org/10.1016/j.jmmm.2019.165494.

[56] C. Kaliyaperumal, S. Jayabalan, A. Sanbarkumar and T. Paramasivam, Solid State Sci. 105, 106245 (2020) And JCPDS File No. 130187 (https://doi.org/10.1016/j.solidstatesciences.2020.106245.

[57] JCPDS File No. 750076/.

[58] H. Tinwala, D. V. Shah, J. Menghan and R. Pati, J. Nanosci. Nanotechno. 14(8), 6072 (2014); https://doi.org/10.1166/jnn.2014.8834.

[59] S.A. Chartier, G. Catillon and J.P. Crocombette, Phys. Rev. Lett. 102, 155503 (2009); https://doi.org/10.1103/PhysRevLett.102.155503.

[60] N. Izu, T. Omata and S. Otsuka–yoo–Ma tsuo, J. Alloys compd. 270, 107 (1998); https://doi.org/10.1016/S0925-8388(98)00464-2.

[61] M.A. Subramanian, G. Aravamudan and G.V. Rao, Prog. Solid State chem. 15, 55 (1983) (https://doi.org/10.1016/0079-6786(83)90001-8.

[62] L. Minervini, R.W. Grims and K.E. Stickafus, J. Am. Ceram. Soc. 83, 1873 (2000); https://doi.org/10.1111/j.1151-2916.2000.tb01484.x.

[63] R.D. Shannon Acta Crystallographica section A. 32(5), 751 (1976); https://doi.org/10.1107/s0567739476001551.

[64] H. Yamamura, H. Nishino, K. Kakinuma and K. Nomura, J. Ceram. Soc. Jpn. 111, 902 (2003); https://doi.org/10.2109/jcersj.111.902.

[65] JCPDS File No.461508.

[66] B.P. Mandal, N. Gerg, S.M. Sharma and A.K. Tyagi, J. Solid State Chem. 179, 1990 (2006); https://doi.org/10.1016/j.jssc.2006.03.036.

[67] V. Esposito, B.H. Luong, E.D. Bartolomeo, E.D. Wachsman and E. Traversa, J. Electrochem.Soc. 153, A 2232 (2006); https://doi.org/10.1149/1.2358088.

[68] Q.A. Wang, H. wang and X. Yao, J. Appl. Phys.101, 104116 (2007); https://doi.org/10.1063/1.2735409.

[69] J.F. Vente, R.B. Helmholdt and D.J.W. Ijdo, J. Solid State Chem. 108, 18 (1994); https://doi.org/10.1006/jssc.1994.1003.

[70] N.P. Klug and A.E. Alexander, X-ray diffraction procedure (Wiley Interscience, New York, 1954.

[71] K. Ravichandran, D. Nedumaran, Int. J. Mech. Eng. Mater. Sci. 4(1), 25 (2011.

[72] X. Gong, P. Wu, W. Chen and H. Yang, J. Mater. Res 13, 469 (1998); https://doi.org/10.1557/JMR.1998.0061.

[73] B. Jezowwka, Trezebinaptz 'Rare Earth Spectroscopy' (world Scientific Publishing Co. Hong Kong, Singapore Ltd.1984) P. 455.

[74] N.F. Mott and E.A. Davis, Electronic Processes in Non-crystalline materials (Clarendon, Oxford, 1971); https://doi.org/10.1002/crat.19720070420.

[75] P.A. Cox, J.B. Goodenough, P.J. Tavener, D. Telles and R.G. Egdell, J. Solid State Chem. 62, 360 (1986); https://doi.org/10.1016/0022-4596(86)90251-3.

[76] H. Yamamura, H. Nishino, K. Kakinumo and N, Nomura, J. Ceram. Soc. Japan 111, 902 (2003); https://doi.org/10.2109/jcersj.111.902.

[77] P.J. Wilde and C.R.A. Catlow, Solid State Ionics 112, 173 (1998); https://doi.org/10.1016/S0167-2738(98)00190-8.

[78] J.C. Maxwell, 'Electricity and Magnetism' vol.1 (Oxford University Press, Oxford, (1973) p.828.

[79] K.W. Wagner, Ann.Phys.40, 817 (1913.

[80] G.Y. Ahm, S.I. Park, I.B. Shim and C.S. Kim, J. Magn.Magn. Mater. 282, 166 (2004); https://doi.org/10.1016/j.jmmm.2004.04.039.

[81] K. Sato and H. Katayama-Yoshida, Semicond. Sci. Technol. 17, 367 (2002); http://dx.doi.org/10.1088/0268-1242/17/4/309.

[82] D.P. Norton, S.J. Pearton, A.F. Hebard, N. Theodoropoulou, L.A. Boatner, R.G. Wilson, Appl. Phys. Lett. 82, 239 (2003); https://doi.org/10.1063/1.1537457.

[83] D. Iusan, B. Sanyal, O. Eriksson, Phys. Rev. B 74, 235208 (2006); https://doi.org/10.1103/PhysRevB.74.235208.

[84] J. Gurgul, M. Rams, Z. Swiatkowska, R. Kmiec and K. Tomala, Phys. Rev. B 75, 64426 (2007); https://doi.org/10.1103/PhysRevB.75.064426.

[85] Y. Shimakawa, Phys.Rev.B 59, 1249 (1999); https://doi.org/10.1103/PhysRevB.59.1249.

[86] M.A. Subramanian, J. Solid state chem. 72, 24 (1988); https://doi.org/10.1016/0022-4596(88)90004-7.

М.Б. Ханвілкар[1,2], А.К. Нфкумбх[2], С.М. Патанж[3], Р.А. Павар[2], Н.Й. Карал[2], Д.В. Нігхот[2], П.А. Нагвад[2], М.Д. Сангале[2], Дж.С. Гугале[2]

Структурні, електричні та магнітні властивості заміщених наночастинок оксиду пірохлору, синтезованих методом спільного осадження

[1]К.М.С. коледж, Хополі, Тал-Халапур, Райгад, Індія, mb.khanvilkar@gmail.com
[2]Університет Савітрібай Фуле Пуни (кол. університет Пуни), Ганешкхінд, Пуна, Індія, aknik1952@gmail.com
[3]Шрікрішна Махавідялая, Гуньойоті, Тал- Омерга, Османабад, Індія, smpatange@rediffmail.com

Методом спільного осадження синтезовано п'ять заміщених нанооксидів пірохлору: $Nd_{1.9}Ho_{0.1}Zr_{1.8}Ce_{0.2}O_7$, $La_{1.95}Ce_{0.05}Zr_{0.29}Ce_{1.71}O_7$, $Y_{1.79}Pr_{0.21}Ru_{1.99}Pr_{0.01}O_7$, $Dy_{1.9}Yb_{0.1}Mn_{1.93}Cu_{0.07}O_7$ and $Dy_{1.99}Sr_{0.01}Sn_2O_7$. Прекурсори контролювали термічними дослідженнями (TGA-DTA). Приготовані нанорозмірні заміщені оксиди пірохлору вивчалт за допомогою EDS, XRD, SEM, TEM, а також досліджували електропровідність, термоелектричну потужність, ефект Холла, діелектричні властивості та вимірювання намагніченості. За допомогою XRD підтверджено утворення однофазних кристалічно заміщених пірохлорів з кубічною природою наночастинок. Для всіх заміщених сполук була прийнята стабільна пірохлорна структура із $r_A^{3+}/r_B^{4+} = 1.395$, за винятком сполуки $La_{1.95}Ce_{0.05}Zr_{0.29}Ce_{1.71}O_7$, для якої $r_A^{3+}/r_B^{4+} = 1.175$, що вказує на порушення пірохлорної структури (тобто флюоритової структури). Температурна залежність електричної провідності для всіх заміщених пірохлорів має два чіткі нахили з розривом. Цей розрив можна віднести до суто напівпровідникових властивостей. Вимірювання термоелектричної потужності та ефекту Холла для всіх сполук підтвердили р-типу для всіх напівпровідників, окрім сполуки $Y_{1.79}Pr_{0.21}Ru_{1.99}Pr_{0.01}O_7$, і яка характеризувалася n-типом провідності. Діелектрична проникність (ε') та діелектричні втрати ($\tan \delta$) коефіцієнта дисипації зменшуються зі збільшенням частот і досягненням постійного значення за певних частот. Застосована польова залежність кривої намагніченості при кімнатній температурі (300 К) для $Nd_{1.9}Ho_{0.1}Zr_{1.8}Ce_{0.2}O_7$, $Y_{1.79}Pr_{0.21}Ru_{1.99}Pr_{0.01}O_7$ та $Dy_{1.9}Yb_{0.1}Mn_{1.93}Cu_{0.07}O_7$, показала петлю гістерезису із петлею з невеликим зламом, який можна віднести до малого, але певного феромагнітного впорядкування поряд із значними парамагнітними та суперпарамагнітними компонентами Намагніченість при 2К показала чіткий цикл гістерезису для пірохлорів $Dy_{1.9}Yb_{0.1}Mn_{1.93}Cu_{0.07}O_7$ та $Dy_{1.99}Sr_{0.01}Sn_2O_7$, які можна вважати слабкими феромагнетиками.

Ключові слова: заміщені оксиди пірохлорного типу, феромагнетизм, електропровідність, намагніченість, обмінна взаємодія, спільне осадження.